Title: Mucosal B cell memory selection integrates tissue-specific microbial cues via the IgA BCR

Authors: Maria Pia Holgado[1,†], Samuel Origlio[1,†], Lucas Bertoia[1], Myriam Moussa[1], Apurwa Trivedi[1], Frederic Fiore[2], Ana Zarubica[2], Emma Slack[3], Michelle A. Linterman[4], Michel Cogné[5], Claude Gregoire[1], Mauro Gaya[1,*]

Affiliations:

[1]Centre d'Immunologie de Marseille-Luminy (CIML), Aix Marseille Université, INSERM, CNRS; Marseille, France.

[2]Centre d'Immunophénomique (CIPHE), Aix Marseille Université, INSERM, CNRS, PHENOMIN, Celphedia; Marseille, France.

[3]Institute of Food, Nutrition and Health, Department of Health Sciences and Technology, ETH Zurich; Zürich, Switzerland.

[4]Immunology Program, Babraham Institute; Cambridge, UK.

[5]Rennes University, INSERM; Rennes, France.

[†]These authors contributed equally

* Correspondence: gaya@ciml.univ-mrs.fr (M.G.)

Abstract

B cells engender long-lived plasma cells (LLPCs) and memory B cells (MBCs) to combat recurrent pathogens. While B cell receptor (BCR) affinity dictates fate decisions in clonally-restricted set-ups, the driving factors in more complex systems remain unknown. Here, we show that memory selection during mucosal infection is imprinted by inherent cues from barrier tissues: lungs skew selection towards MBCs while the gut favors LLPC entry, even in response to the same pathogen. This divergence is linked to differential BCR isotype usage across barrier tissues rather than to affinity. In the gut, the commensal-induced TGF-β-rich milieu promotes B cell class-switching to IgA. Consequently, the IgA BCR bias selection towards LLPCs, a process that is counteracted by its cytosolic tail domain. Overall, mucosal B cell selection integrates tissue-specific microbial cues by strongly relying on BCR isotype usage rather than affinity, with implications for nasal and oral vaccine development.

One sentence summary: Divergent B cell memory strategies evolved in lung and gut mucosa to counteract recurrent pathogens.

Main text:

Introduction

One of the main facets of vertebrates' immune system is the ability to remember previously encountered pathogens through a process known as immunological memory. This strategy involves the generation of long-lasting memory cell populations derived from B and T lymphocytes. In particular, B cells can give rise to two different memory compartments: long-lived plasma cells (LLPCs), which constitutively secrete antibodies throughout life, and memory B cells (MBCs), which remain in quiescent state but can rapidly differentiate into antibody-secreting cells upon antigen re-exposure, complementing existing humoral immunity (*1*). MBCs and LLPCs are the basis of vaccination, therefore, deciphering the cellular and molecular mechanisms that drive B cell selection into the LLPC and MBC programs is of utmost interest.

Previous work using immunization with model antigens or clonally restricted B cell systems, showed that BCR affinity plays a key role in determining memory cell fate: high affinity B cells preferentially differentiate into LLPCs while the MBC compartment is less stringent, allowing for the entry of low-affinity cells and supporting memory diversity (*2*–*4*). Recent work revealed that immunization with complex antigens supports the output of low- and high affinity LLPCs, suggesting that affinity is not the only factor driving the LLPC program when multiple B cell clones with distinct BCR specificities coexist (*5*, *6*).

Unlike systemic immunization with model antigens, mucosal infection gives rise to B cells with various specificities and BCR isotypes (IgM, IgG and IgA) that take up residence not only in lymphoid organs but also in barrier tissues such as lungs (*7*–*11*) and gut (*12*–*16*). This raises the question of the mechanisms that dictate B cell memory selection in such scenarios. Here, we used respiratory and gastrointestinal infection models to investigate the mechanisms instructing B cell memory in the mucosas. We found that inherent features from barrier tissues alternately skews B cell selection towards MBCs in the lungs and LLPCs in the gut. Limiting affinity maturation by means of loss-of-function mutation in Aid did not impact memory cell fate. Instead, differential BCR isotype expression across barrier tissues accounts for the tissue-specific biased selection. We found that preferential usage of IgA BCRs in the gut, fostered by a comensal-induced TGF-β-rich milieu, fine-tunes downstream signaling upon antigen encounter and drives B cells into the LLPC program. Then, we propose a model where mucosal B cell memory selection integrates tissue-specific microbial cues by strongly relying on BCR isotype usage rather than affinity.

Results

Divergent B cell memory strategies evolved in lungs and gut

To study B cell memory responses in the mucosas, we used the *Aicda*-cre^{ERT2} *Rosa26*-EYFP (Aid-EYFP) mouse model, which allows to permanently label LLPCs and MBCs based on their precursors' expression of Aid, the enzyme that initiates class switching and somatic hypermutation (*17*). We initially analyze the establishment of B cell memory in the lungs and gut, as these organs are key barriers exposed to the environment and play a central role in orchestrating homeostatic and pathogenic immune responses. To analyze lung B cell memory, we intranasally infected Aid-EYFP mice with influenza A virus PR8 strain and treated them with tamoxifen from day 6 (Figure 1A). After 5 weeks, we harvested lungs and segregated resident YFP^{+} cells into memory and germinal center (GC) cells based on GL7 labeling by flow cytometry. Within the memory population, we found LLPCs and MBCs at a 25:75 ratio, indicating that the B cell memory compartment in the lung barrier is enriched in MBCs (Figure 1B). Both LLPCs and MBCs recognized influenza hemagglutinin and nucleoprotein antigens but segregated in different lung zones: LLPCs formed clusters in the periphery of bronchus-associated lymphoid tissue while MBCs accumulated in the center of these tertiary lymphoid structures (Figures 1C-1E). To assess the stability of this MBC-biased composition, we treated mice as in Figure 1A and sacrificed them 365 days after. We found that MBCs largely outnumber LLPCs in the lung even one year after infection, showing that this MBC-biased strategy is maintained across time once established (Figure S1A). In addition, this experiment confirms that lung MBCs

and LLPCs are indeed long-lived, as they were labelled by tamoxifen during the first month of infection and still found in the lungs 11 months after.

To determine the composition of the B cell memory compartment in the gut mucosa, we orally infected Aid-EYFP mice with *Salmonella typhimurium* SL3261 strain and administered tamoxifen from day 6 post-infection. After 5 weeks, we harvested the small and large intestine and separated YFP^+ cells into memory and GC cells based on GL7 labeling. We found LLPCs and MBCs at a 80:20 ratio, unveiling that the gut memory compartment, in marked contrast to the lung tissue, is largely dominated by LLPCs (Figure 1F). Furthermore, YFP^+ populations were physically segregated within the gut, with GC cells primarily located in Peyer's patches and cecal patches, LLPCs dispersed throughout the small intestinal villi and colonic crypts, and MBCs within both sites (Figures 1G and S1B). Lamina propria-resident LLPCs were antigen-specific, as they recognized *Salmonella* lipopolysaccharide (Figure 1H). Notably, these LLPCs remained active in the gut for extended periods, as we detected LPS-specific antibody-secreting cells in the lamina propria and LPS-specific antibodies in the feces even 250 days post-infection (Figures S1C-S1D).

We next examined the functional implications of these divergent B cell memory strategies in lung and gut barrier tissues. To assess this, we primarily infected mice with either influenza PR8 or *Salmonella* SL3261 strains and rechallenged them at week 5 with influenza A virus HKx31 strain or *Salmonella* SL12023 strain. After 4 days of re-challenge, we measured the formation of antibody-secreting cells in lungs and gut by ELISpot. Secondary infection led to a robust de-novo formation of flu-specific antibody-secreting cells in the lungs while no significant increase in *Salmonella*-specific antibody-secreting cells was observed in the small and large intestines (Figures 1I and 1J). These results are in line with the notion that lung MBCs can rapidly differentiate into antibody-secreting cells to deal with influenza variants while the gut relies on antibodies produced by gut-resident LLPCs elicited during primary infection to rapidly cope with a secondary *Salmonella* encounter.

To determine whether the marked differences in B cell memory strategies observed in the lung and gut barriers are due to the type of pathogen used in each setup or inherent features of the barrier site, we infected Aid-EYFP mice with the same pathogen, *Klebsiella pneumoniae*, either intranasally or orally. We found that intranasal *Klebsiella* infection elicited an MBC-biased response in the lungs, whereas oral *Klebsiella* infection triggered an LLPC-biased response in the small and large intestines, demonstrating that these differences are not pathogen-related (Figures 1K and S1E-S1F). Notably, the number of *Klebsiella*-specific LLPCs in the bone marrow was comparable between groups receiving *Klebsiella* intranasally or orally, indicating that the MBC-biased response in the lungs is not due to preferential migration of LLPCs to the bone marrow (Figures S1G-S1H). Instead, our results show that divergent B cell memory strategies have evolved in the lungs and gut to cope with potential future threats.

Selection in GCs shapes lung and gut B cell memory compartments

Next, we wondered whether contrasting B cell memory strategies in the lung and gut mucosa were associated with a differential output of PCs and MBCs during GC selection. To assess this, we tracked the number of $CD138^+$ and $CD38^+CCR6^+$ cells within the $CD19^+GL7^+Fas^+$ GC population in lung- and gut-draining lymph nodes following intranasal or oral infection with *Klebsiella pneumoniae*. The $CD138^+$ population represents pre-PCs (*18*), while the $CD38^+CCR6^+$ population is highly enriched in pre-MBCs, as further confirmed by their high expression of CXCR3 (Figures 2A and S2A) (*19*, *20*). Interestingly, when we measured the ratio of pre-PCs to the pre-MBC-enriched population, we found that this ratio was consistently higher at all time points in gut-draining lymphoid organs than in lung-draining ones (Figures 2A and S2B). These findings suggest that GCs in gut-associated lymph nodes exhibit a preferential bias toward the production of PCs compared to those in the lung. We further confirmed this pattern using our influenza and *Salmonella* infection models, where the pre-PC/pre-MBC output ratio remained elevated in gut-draining

organs (Figures 2B and S2C). Overall, our results indicate that the enrichment of LLPCs within the gut memory B cell compartment is due, at least in part, to a favored selection of pre-PCs during GC reactions.

During infection, B cell selection can occur not only within GCs but also through extrafollicular pathways (*21*). To assess to what extent the observed differences in memory commitment within GCs contribute to divergent memory strategies in the lungs and gut, we genetically disrupted GC formation by deleting the transcription factor Bcl6 in B cells (*22*). For this, we crossed Bcl6$^{fl/fl}$ mice with either CD19-cre or CD23-cre lines and infected the resulting animals with influenza virus or *Salmonella*. In CD19-cre^{+}Bcl6$^{fl/fl}$ mice, incomplete deletion of Bcl6 did not prevent GC formation or memory responses, likely due to selective expansion of B cells that escaped deletion (Figures S2D–S2H). In contrast, CD23-cre^{+} Bcl6$^{fl/fl}$ mice showed efficient deletion of Bcl6 in B cells, resulting in a marked reduction of GC structures in the lung and mediastinal lymph nodes following influenza infection (Figures 2C and S2I). This GC disruption led to a strong reduction in lung-resident CXCR3^{+} MBCs specific for influenza hemagglutinin and nucleoprotein, as well as reduced influenza-specific antibody levels in bronchoalveolar lavage fluid (Figures 2D–2E and S2J). These data indicate that GC reactions are required for the generation of lung MBCs and local antibody responses. In the gut, CD23-cre^{+} Bcl6$^{fl/fl}$ mice also exhibited a complete loss of GCs in Peyer's patches and mesenteric lymph nodes after *Salmonella* infection (Figures 2F and S2K). Despite *Salmonella*'s known capacity to elicit strong extrafollicular responses (*23*, *24*), we observed a significant reduction in LPS-specific gut LLPCs and fecal antibody titers in these mice (Figures 2G–2H and S2L), suggesting that GC output still contributes significantly to the generation of gut-resident LLPCs, even when extrafollicular responses are active. Altogether, GC selection plays a central role in the formation of mucosal B cell memory compartments in both the lung and gut.

Mucosal memory selection highly relies on BCR isotype usage

Mucosal infections trigger GC reactions that not only comprise B cells with diverse BCR affinities, as observed in conventional immunization models, but also B cells expressing different BCR specificities and isotypes such as IgM, various IgG subclasses, and IgA (*25–28*). To assess the importance of these BCR features in LLPC versus MBC selection in mucosal tissues, we analyzed B cell memory responses in Aid-KO mice, which generate a diverse BCR repertoire but are unable to undergo affinity maturation or isotype class switching (Figures S3 and S4A–S4B). We found that AID deficiency led to a marked reduction in the LLPC:MBC ratios in both the lung and gut following influenza and *Salmonella* infection, respectively (Figures 3A–3B and S4C–S4D). These results indicate that affinity maturation and/or class switching are critical for memory selection during mucosal infection. To disentangle the contribution of these two processes, we used Aid(G23S) mutant mice, which carry a point mutation in AID that impairs somatic hypermutation while preserving class switching (Figures S3E–S3F) (*29*). Intriguingly, LLPC:MBC ratios in wild-type and Aid(G23S) mice were comparable following influenza or *Salmonella* infection (Figures 3C–3D and S4G–S4H), indicating that limiting affinity maturation does not impact LLPC vs. MBC fate decision in these barrier tissues.

Based on these results, we hypothesized that class switching towards different BCR isotypes could play a dominant role in dictating B cell memory selection at mucosal sites. To test this, we measured the BCR isotype landscape in the memory compartment after 35 days of influenza or *Salmonella* infection. We found that IgG^{+} B cells could seed the MBC and LLPC compartments to a similar extent. In contrast, B cells that underwent class-switching towards IgA were mostly selected towards the LLPC compartment rather than to the MBC one (Figures 3E and 3F). This phenomenon was not due to differential organ distribution of IgA^{+} LLPCs and MBCs, as we obtained similar findings in secondary lymphoid organs and barrier tissues (Figures S4I-S4J). Instead, our results are in line with a model where the IgA BCR favors B cell entry into the LLPC program.

To assess if the expression of the IgA BCR itself can bias selection towards the LLPC pathway, we used α1KI transgenic mice in which IgA expression is genetically driven by the insertion of the IgA constant

region in place of the IgM (*30*). We further crossed α1KI mice with *Aid*-KO animals in order to block somatic hypermutation and subsequent class-switching towards other isotypes (Figures S4K and S4L). We infected wild type, *Aid*-KO and *Aid*-KO/α1KI animals either with influenza virus or *Salmonella* and measured B cell memory responses after 35 days. We found that forced expression of the IgA BCR fully recovered the hindered LLPC differentiation observed in *Aid*-KO mice, in both lungs and gut (Figures 3G-3H and S4M-S4N). These results demonstrate that the IgA BCR itself biases B cell selection towards the LLPC program regardless of affinity or other extrinsic factors, and reveal that mucosal memory selection is strongly driven by BCR isotype usage rather than affinity.

Mucosal memory selection integrates microbial cues via the IgA BCR

Given the key role of the IgA BCR in driving mucosal B cell selection, we hypothesized that the distinct memory strategies observed in the lung and gut might result from differential usage of the IgA BCR during GC reactions in these tissues. To test this, we analyzed IgA BCR isotype usage among GC B cells in lung- and gut- lymphoid structures and draining lymph nodes following intranasal or oral *Klebsiella* infection. We found that class switching to IgA was ten times more frequent in Peyer's patches than in the lungs and twice as frequent in mesenteric lymph nodes compared to mediastinal lymph nodes (Figures 4A-4B). Similar patterns of increased IgA usage in the gut compartment relative to the lung were observed in our influenza and *Salmonella* infection models (Figure 4C), suggesting that elevated IgA class switching in gut-associated GC reactions may contribute to the enhanced LLPC output in this tissue. To directly assess the role of the IgA BCR in memory cell fate decisions, we infected wild-type and Igha-deficient mice with either influenza virus or *Salmonella* and analyzed B cell memory responses 35 days post-infection. Igha-KO mice exhibited a significant reduction in LLPC output in both infection models (Figures 4D-4E and S5A-S5B). Interestingly, these mice also displayed increased numbers of IgM-secreting cells, possibly reflecting a compensatory response in the absence of IgA (Figures S5C-S5D). Altogether, these findings support a model in which the IgA BCR promotes LLPC differentiation, and suggest that the extent of IgA BCR usage within GC reactions plays a key role in shaping the type of memory response established at mucosal sites during infection.

Class-switching towards IgA is primarily driven by TGF-β, a cytokine produced in response to microbial colonization (*31–35*). We hypothesized that the high microbiota biomass in the intestine contributes to the elevated IgA class switching observed in gut-associated GC reactions. To test this, we compared TGF-β levels in germ-free and specific-pathogen-free (SPF) mice. While TGF-β levels in lung-draining lymph nodes were similar between the two groups, Peyer's patches of germ-free mice showed significantly reduced TGF-β levels compared to SPF controls (Figure 4F). To evaluate the functional relevance of the microbiota–TGF-β axis in shaping B cell memory responses, we infected both germ-free and SPF mice with influenza virus or Salmonella. Consistent with the TGF-β findings, IgA class switching in the lungs occurred at comparable levels in both groups (Figures 4G and S5E). Conversely, class switching to IgA was markedly reduced in Peyer's patches of germ-free mice (Figures 4G and S5F). In addition, LLPC:MBC output in the lungs remained similar between germ-free and SPF mice, whereas germ-free animals exhibited a significantly lower LLPC:MBC ratio in the gut following Salmonella infection (Figures 4H-4I and S5G-S5H). These findings suggest that the elevated microbial load in the gut promotes TGF-β production and IgA class switching, thereby biasing B cell memory selection toward the LLPC fate during mucosal infection.

To directly test whether the microbiota–TGF-β axis shapes gut memory responses through B cell–intrinsic TGF-β sensing, we generated mice lacking the TGF-β receptor II specifically in B cells (CD19-Cre^{+} Tgfbr2$^{fl/fl}$). Then, we infected CD19-Cre^{+} and Cre^{-} Tgfbr2$^{fl/fl}$ mice with *Salmonella*. In CD19-Cre^{+} Tgfbr2$^{fl/fl}$ mice, we did not observe IgA^{+} cells within GC reactions in Peyer's patches, consistent with the notion that TGF-β signaling is essential for IgA class switching (Figure 4J). Remarkably, the strong LLPC bias typically

observed in the gut was partially reversed in the absence of TGF-β signaling in B cells (Figures 4K and S5I). These findings support a model in which mucosal memory selection integrates tissue-specific microbial cues through TGF-β signaling and IgA BCR usage, driving distinct B cell memory outcomes in the gut versus the lung.

The IgA BCR relies on its cytosolic tail to amplify BCR signalling

The strength of BCR signaling plays a pivotal role in determining B cell fate upon antigen recognition (*36–38*). A recent study further demonstrated that the IgA BCR transmits signals of different magnitude compared to other isotypes (*39*). Based on this, we hypothesized that selectively altering IgA BCR signaling could modulate mucosal B cell selection and the LLPC:MBC output during infection. To test this, we aimed to selectively manipulate IgA BCR signaling without affecting other isotypes. Class-switched BCRs (IgG and IgA), unlike those on naïve B cells (IgD and IgM), contain a conserved cytoplasmic tail across species (*40*). While previous studies have shown that the IgG tail enhances BCR signaling (*41*, *42*), the functional role of the IgA tail, and whether it contributes to signal strength, remains unknown. To begin addressing this, we genetically engineered GC-like IgG2a$^+$ A20 B cells to express an IgA BCR by introducing CRISPR-Cas9 guide RNAs targeting the Sγ2a-3' and Sα-3' switch regions (*43*) (Figure 5A). This strategy was highly efficient in forcing class-switching from IgG to IgA while preserving surface BCR expression, as confirmed by anti-kappa light chain staining (Figures 5B-5C). We then generated IgA$^+$ B cells lacking the cytoplasmic tail sequence (RGPFGSKEVPQY) using CRISPR-Cas9. To facilitate identification of successful recombinants, we inserted P2A and CD90.1 coding sequences into both wild-type and Δtail constructs (Figure 5D). Notably, deletion of the tail did not affect membrane expression of IgA (Figures 5E–5F).

To evaluate the functional relevance of the IgA tail in BCR signaling, we performed a series of assays. First, calcium flux analysis revealed that Δtail IgA$^+$ B cells displayed reduced calcium mobilization compared to wild-type cells following cross-linking with increasing concentrations of anti-IgA antibody, while both B cells responded similarly to ionomycin (Figure 5G). Next, we assessed global phosphorylation using anti-phosphotyrosine (4G10) western blotting and observed a marked reduction in the phosphorylation landscape of Δtail IgA$^+$ B cells upon BCR cross-linking (Figure 5H). Finally, phospho-flow cytometry showed significantly reduced phosphorylation of early signaling molecules Btk and Syk in Δtail IgA$^+$ B cells upon stimulation (Figures 5I-5J). Altogether, these findings demonstrate that the cytoplasmic tail of the IgA BCR is required for effective signaling upon antigen engagement. Its removal selectively impairs IgA BCR signaling, providing a tool to specifically modulate this pathway without affecting other isotypes.

The IgA BCR cytosolic tail shapes mucosal B cell memory responses

To assess to which extent IgA BCR signalling can impact B cell memory selection, we generated new transgenic mice in which we introduced a P2A-tdTomato cassette at the end of the IghA coding sequence to track IgA$^+$ cells (Igha-tdTom) and subsequently deleted the cytosolic tail domain (Igha-Δtail-tdTom) (Figure 6A). Labeling was highly efficient in both mouse strains, as IgA$^+$ GCs, MBCs and LLPCs expressed high levels of tdTomato in lungs and gut upon infection (Figures 6B and 6C). Yet, some IgA$^-$ cells, in particular LLPCs, expressed considerable levels of tdTomato, although to a lesser extent than IgA$^+$ cells. This phenomenon might be due to expression of IgA germline transcripts in IgG$^+$ cells and/or switch transcripts from the nonproductive heavy-chain allele, as previously observed in IgE-GFP mice (*44*).

We next tested whether removal of the IgA cytoplasmic tail affects BCR signaling in primary B cells. To do this, we stimulated IgA$^+$ GC B cells from Igha-tdTom and Igha-Δtail-tdTom Peyer's patches with anti-IgA antibody and measured Btk phosphorylation by phospho-flow cytometry. In line with our earlier results from GC-like B cell lines, deletion of the IgA cytoplasmic tail significantly reduced Btk phosphorylation upon BCR stimulation, confirming that the IgA BCR requires its cytosolic tail to effectively transduce signaling (Figure 6D). We then assessed the functional consequences of reduced BCR signaling on B cell memory selection.

Surprisingly, IgA$^+$ cells from Igha-Δtail-tdTom mice were more efficiently selected into the LLPC pathway than those from Igha-tdTom counterparts, in both the lungs and gut following influenza or Salmonella infection, respectively (Figures 6E-6F). This enhanced LLPC differentiation was accompanied by significantly elevated pathogen-specific IgA levels in serum and feces (Figures 6G-6H).

To further validate our findings in a competitive setting, we took advantage of allelic exclusion, a mechanism by which B cells express only one heavy chain locus during development. We analyzed heterozygous Igha-tdTom$^+$/$^-$ and Igha-Δtail-tdTom$^+$/$^-$ mice, which generate two genetically distinct populations of IgA$^+$ B cells: one expressing wild-type IgA and the other expressing either IgA-tdTom or IgA-Δtail-tdTom. Using tdTomato fluorescence, we were able to distinguish IgA$^+$ cells derived from the modified versus wild-type alleles (Figures S6A-S6B). We infected these heterozygous mice with influenza or Salmonella and analyzed IgA$^+$ cells in the memory compartments 35 days later. In both lungs and gut, we observed that Igha-Δtail-tdTom$^+$ cells were consistently enriched in the LLPC compartment and underrepresented in the MBC compartment compared to Igha-tdTom$^+$ cells (Figures S6A-S6B). These results exclude the possibility that external factors are responsible for the enhanced LLPC output of IgA$^+$ B cells lacking the cytosolic tail. Instead, our results support the notion that intrinsic differences in BCR signaling underlie divergent memory fates.

Although these results were initially unexpected, recent studies have shown that BCR signaling in GC B cells must be tightly regulated to prevent excessive accumulation of reactive oxygen species (ROS) and subsequent cell death (*45*). For instance, enhanced BCR signaling resulting from phosphatase deletion in IgG$^+$ GC B cells leads to increased oxidative stress, which impairs PC differentiation (*45*, *46*). To determine whether the increased PC output observed in Igha-Δtail mice was linked to reduced oxidative stress, we measured mitochondrial ROS levels using MitoSOX staining and apoptosis using caspase-3 staining in IgA$^+$ GC B cells of Igha-tdTom and Igha-Δtail-tdTom mice. We found that IgA$^+$ cells lacking the cytoplasmic tail accumulated less ROS upon BCR cross-linking and exhibited fewer caspase-3$^+$ cells, indicating reduced apoptosis (Figures 6I-6J). Altogether, our findings suggest that the cytoplasmic tail of the IgA BCR modulates signaling strength and fine-tunes B cell memory selection during mucosal infection.

Discussion

B cell memory responses at barrier tissues provide rapid and efficient protection against mucosal pathogens (*47–51*). In our study, we uncovered that distinct B cell memory strategies evolved in lungs and gut to counteract recurrent pathogens. Memory selection is skewed towards MBCs in the lungs while a strong LLPC-bias exists in the gut. We found that this divergence is linked to differential BCR isotype usage across barrier tissues rather than to affinity. In the gut, the high microbiota content fosters a regulatory environment rich in TGF-β and Treg cells that prevent excessive immune reactions to commensal bacteria while promoting B cell class switching towards IgA (*32*, *52*). In turn, the IgA BCR favors B cell entry into the LLPC program by fine-tuning downstream signaling. These results support a model in which mucosal memory selection integrates tissue-specific microbial cues by highly relying on BCR isotype usage rather than affinity. Furthermore, our findings raise the possibility that the IgA- and LLPC-biased memory response in the gut is a by-product of evolutionary pressures that have shaped a regulatory environment in the gut to limit the immune system's activation against the resident microbiota.

What features of the IgA BCR could promote B cell differentiation into LLPCs? A previous study demonstrated that IgA transmits signals of different magnitude compared to IgG (*39*), leading us to hypothesize that dampening this signaling would impair PC differentiation. Unexpectedly, we observed the opposite: genetic deletion of the IgA cytoplasmic tail reduced BCR signaling but increased the bias toward LLPC formation. Although counterintuitive, this finding aligns with recent studies showing that excessive BCR signaling in GC B cells impairs their selection and PC differentiation due to elevated ROS production and intracellular calcium release (*45*, *46*, *53*, *54*). Beyond the cytoplasmic tail, other molecular features of the IgA BCR may also influence B cell responsiveness and fate decisions. For example, the organization of

the BCR within the plasma membrane has been shown to differ among isotypes such as IgM, IgD, and IgG (*55*, *56*), yet remains unexplored for IgA. In addition, the distinct structural properties of the IgA hinge region may further contribute to its functional specificity. These possibilities are currently being investigated in our laboratory and will be the focus of future research.

Finally, our results prompt us to consider the potential benefit of having two alternative memory strategies in different barrier tissues. In the gut, where we are occasionally exposed to pathogens through poisoned food and water, including *E. coli*, *Salmonella*, *Shigella*, *Rotavirus* and *Norovirus*, a memory response based on antibodies produced by lamina propria-resident LLPCs might be beneficial for the rapid opsonization and elimination of these pathogens from the gut lumen upon re-encounter (*13*, *57*). Conversely, in the lungs, we are frequently exposed to airborne viruses that rapidly spread through the community and generate new variants every season. In this context, it is advantageous to have a population of tissue-resident MBCs with broader antigen affinities that can recognize viral variants, thereby complementing the humoral immunity provided by lung LLPCs (*58*, *59*). These different B cell memory strategies employed by the lungs and the gut are key factors to consider when developing effective nasal and oral vaccines against mucosal pathogens.

References

1. M. Akkaya, K. Kwak, S. K. Pierce, B cell memory: building two walls of protection against pathogens. *Nat. Rev. Immunol.* **20**, 229–238 (2020).

2. K. G. Smith, A. Light, G. J. Nossal, D. M. Tarlinton, The extent of affinity maturation differs between the memory and antibody-forming cell compartments in the primary immune response. *EMBO J.* **16**, 2996–3006 (1997).

3. T. G. Phan, D. Paus, T. D. Chan, M. L. Turner, S. L. Nutt, A. Basten, R. Brink, High affinity germinal center B cells are actively selected into the plasma cell compartment. *J. Exp. Med.* **203**, 2419–2424 (2006).

4. R. Shinnakasu, T. Inoue, K. Kometani, S. Moriyama, Y. Adachi, M. Nakayama, Y. Takahashi, H. Fukuyama, T. Okada, T. Kurosaki, Regulated selection of germinal-center cells into the memory B cell compartment. *Nat. Immunol.* **17**, 861–869 (2016).

5. A. Sprumont, A. Rodrigues, S. J. McGowan, C. Bannard, O. Bannard, Germinal centers output clonally diverse plasma cell populations expressing high- and low-affinity antibodies. *Cell* **186**, 5486–5499.e13 (2023).

6. H. J. Sutton, X. Gao, H. G. Kelly, B. J. Parker, M. Lofgren, C. Dacon, D. Chatterjee, R. A. Seder, J. Tan, A. H. Idris, T. Neeman, I. A. Cockburn, Lack of affinity signature for germinal center cells that have initiated plasma cell differentiation. *Immunity* **57**, 245–255.e5 (2024).

7. N. Swarnalekha, D. Schreiner, L. C. Litzler, S. Iftikhar, D. Kirchmeier, M. Künzli, Y. M. Son, J. Sun, E. A. Moreira, C. G. King, T resident helper cells promote humoral responses in the lung. *Sci Immunol* **6** (2021).

8. H.-X. Tan, J. A. Juno, R. Esterbauer, H. G. Kelly, K. M. Wragg, P. Konstandopoulos, S. Alcantara, C. Alvarado, R. Jones, G. Starkey, B. Z. Wang, O. Yoshino, T. Tiang, M. L. Grayson, H. Opdam, R. D'Costa, A. Vago, Austin Liver Transplant Perfusionist Group, L. K. Mackay, C. L. Gordon, D. Masopust, J. R. Groom, S. J. Kent, A. K. Wheatley, Lung-resident memory B cells established after pulmonary influenza infection display distinct transcriptional and phenotypic profiles. *Sci Immunol* **7**, eabf5314 (2022).

9. N. R. Mathew, J. K. Jayanthan, I. V. Smirnov, J. L. Robinson, H. Axelsson, S. S. Nakka, A. Emmanouilidi, P. Czarnewski, W. T. Yewdell, K. Schön, C. Lebrero-Fernández, V. Bernasconi, W. Rodin, A. M. Harandi, N. Lycke, N. Borcherding, J. W. Yewdell, V. Greiff, M. Bemark, D. Angeletti, Single-cell BCR and transcriptome analysis after influenza infection reveals spatiotemporal dynamics of antigen-specific B cells. *Cell Rep* **41**, 111764 (2022).

10. J. E. Oh, E. Song, M. Moriyama, P. Wong, S. Zhang, R. Jiang, S. Strohmeier, S. H. Kleinstein, F. Krammer, A. Iwasaki, Intranasal priming induces local lung-resident B cell populations that secrete protective mucosal antiviral IgA. *Sci Immunol* **6**, eabj5129 (2021).

11. S. R. Allie, J. E. Bradley, U. Mudunuru, M. D. Schultz, B. A. Graf, F. E. Lund, T. D. Randall, The establishment of resident memory B cells in the lung requires local antigen encounter. *Nat. Immunol.* **20**, 97–108 (2019).

12. B. Zhang, S. Chen, X. Yin, C. D. McBride, J. A. Gertie, M. Yurieva, A. A. Bielecka, B. Hoffmann, J. Travis Hinson, J. Grassmann, L. Xu, E. R. Siniscalco, A. Soldatenko, L. Hoyt, J. Joseph, E. B. Norton, G. Uthaman, N. W. Palm, E. Liu, S. C. Eisenbarth, A. Williams, Metabolic fitness of IgA plasma cells in the gut requires DOCK8. *Mucosal Immunol* **17**, 431–449 (2024).

13. A. Reboldi, T. I. Arnon, L. B. Rodda, A. Atakilit, D. Sheppard, J. G. Cyster, IgA production requires B cell interaction with subepithelial dendritic cells in Peyer's patches. *Science* **352**, aaf4822 (2016).

14. J. H. Fritz, O. L. Rojas, N. Simard, D. D. McCarthy, S. Hapfelmeier, S. Rubino, S. J. Robertson, M. Larijani, J. Gosselin, I. I. Ivanov, A. Martin, R. Casellas, D. J. Philpott, S. E. Girardin, K. D. McCoy, A. J. Macpherson, C. J. Paige, J. L. Gommerman, Acquisition of a multifunctional IgA+ plasma cell phenotype in the gut. *Nature* **481**, 199–203 (2011).

15. E. Slack, S. Hapfelmeier, B. Stecher, Y. Velykoredko, M. Stoel, M. A. E. Lawson, M. B. Geuking, B. Beutler, T. F. Tedder, W.-D. Hardt, P. Bercik, E. F. Verdu, K. D. McCoy, A. J. Macpherson, Innate and adaptive immunity cooperate flexibly to maintain host-microbiota mutualism. *Science* **325**, 617–620 (2009).

16. C. Lindner, I. Thomsen, B. Wahl, M. Ugur, M. K. Sethi, M. Friedrichsen, A. Smoczek, S. Ott, U. Baumann, S. Suerbaum, S. Schreiber, A. Bleich, V. Gaboriau-Routhiau, N. Cerf-Bensussan, H. Hazanov, R. Mehr, P. Boysen, P. Rosenstiel, O. Pabst, Diversification of memory B cells drives the continuous adaptation of secretory antibodies to gut microbiota. *Nat. Immunol.* **16**, 880–888 (2015).

17. S. Le Gallou, Z. Zhou, L.-H. Thai, R. Fritzen, A. V. de Los Aires, J. Mégret, P. Yu, D. Kitamura, E. Bille, F. Tros, X. Nassif, A. Charbit, S. Weller, J.-C. Weill, C.-A. Reynaud, A splenic IgM memory subset with antibacterial specificities is sustained from persistent mucosal responses. *J. Exp. Med.* **215**, 2035–2053 (2018).

18. L. Binet, C. Dong, N. Attaf, L. Gil, M. Fallet, T. Boudier, B. Escalière, L. Chasson, C. Siret, S. Van de Pavert, J.-M. Navarro, P. Milpied, Specific pre-plasma cell states and local proliferation at the dark zone - medulla interface characterize germinal center-derived plasma cell differentiation in lymph node, *bioRxiv* (2024). https://doi.org/10.1101/2024.07.26.605240.

19. D. Suan, N. J. Kräutler, J. L. V. Maag, D. Butt, K. Bourne, J. R. Hermes, D. T. Avery, C. Young, A. Statham, M. Elliott, M. E. Dinger, A. Basten, S. G. Tangye, R. Brink, CCR6 Defines Memory B Cell Precursors in Mouse and Human Germinal Centers, Revealing Light-Zone Location and Predominant Low Antigen Affinity. *Immunity* **47**, 1142–1153.e4 (2017).

20. N. M. Arroyo-Díaz, H. Bachus, A. Papillion, T. D. Randall, J. Akther, A. F. Rosenberg, B. León, A. Ballesteros-Tato, Interferon-γ production by Tfh cells is required for CXCR3 pre-memory B cell differentiation and subsequent lung-resident memory B cell responses. *Immunity* **56**, 2358–2372.e5 (2023).

21. R. A. Elsner, M. J. Shlomchik, Germinal Center and Extrafollicular B Cell Responses in Vaccination, Immunity, and Autoimmunity. *Immunity* **53**, 1136–1150 (2020).

22. W. S. Foster, J. L. Lee, N. Thakur, J. Newman, A. J. Spencer, S. Davies, D. Woods, L. Godfrey, I. M. Hay, S. Innocentin, J. C. Yam-Puc, E. C. Horner, H. J. Sharpe, J. E. Thaventhiran, D. Bailey, T. Lambe, M. A. Linterman, Tfh cells and the germinal center are required for memory B cell formation & humoral immunity after ChAdOx1 nCoV-19 vaccination. *Cell Rep Med* **3**, 100845 (2022).

23. R. Di Niro, S.-J. Lee, J. A. Vander Heiden, R. A. Elsner, N. Trivedi, J. M. Bannock, N. T. Gupta, S. H. Kleinstein, F. Vigneault, T. J. Gilbert, E. Meffre, S. J. McSorley, M. J. Shlomchik, Salmonella Infection Drives Promiscuous B Cell Activation Followed by Extrafollicular Affinity Maturation. *Immunity* **43**, 120–131 (2015).

24. A. F. Cunningham, F. Gaspal, K. Serre, E. Mohr, I. R. Henderson, A. Scott-Tucker, S. M. Kenny, M. Khan, K.-M. Toellner, P. J. L. Lane, I. C. M. MacLennan, Salmonella induces a switched antibody response without germinal centers that impedes the extracellular spread of infection. *J. Immunol.* **178**, 6200–6207 (2007).

25. Y. Adachi, T. Onodera, Y. Yamada, R. Daio, M. Tsuiji, T. Inoue, K. Kobayashi, T. Kurosaki, M. Ato, Y. Takahashi, Distinct germinal center selection at local sites shapes memory B cell response to viral escape. *J Exp Med* **212**, 1709–1723 (2015).

26. A. E. Denton, S. Innocentin, E. J. Carr, B. M. Bradford, F. Lafouresse, N. A. Mabbott, U. Mörbe, B. Ludewig, J. R. Groom, K. L. Good-Jacobson, M. A. Linterman, Type I interferon induces CXCL13 to support ectopic germinal center formation. *J Exp Med* **216**, 621–637 (2019).

27. C. R. Nowosad, L. Mesin, T. B. R. Castro, C. Wichmann, G. P. Donaldson, T. Araki, A. Schiepers, A. A. K.

Lockhart, A. M. Bilate, D. Mucida, G. D. Victora, Tunable dynamics of B cell selection in gut germinal centres. *Nature* **588**, 321–326 (2020).

28. H. W. King, N. Orban, J. C. Riches, A. J. Clear, G. Warnes, S. A. Teichmann, L. K. James, Single-cell analysis of human B cell maturation predicts how antibody class switching shapes selection dynamics. *Sci Immunol* **6** (2021).

29. M. Wei, R. Shinkura, Y. Doi, M. Maruya, S. Fagarasan, T. Honjo, Mice carrying a knock-in mutation of Aicda resulting in a defect in somatic hypermutation have impaired gut homeostasis and compromised mucosal defense. *Nat. Immunol.* **12**, 264–270 (2011).

30. S. Duchez, R. Amin, N. Cogné, L. Delpy, C. Sirac, V. Pascal, B. Corthésy, M. Cogné, Premature replacement of mu with alpha immunoglobulin chains impairs lymphopoiesis and mucosal homing but promotes plasma cell maturation. *Proc. Natl. Acad. Sci. U. S. A.* **107**, 3064–3069 (2010).

31. B. B. Cazac, J. Roes, TGF-beta receptor controls B cell responsiveness and induction of IgA in vivo. *Immunity* **13**, 443–451 (2000).

32. K. Atarashi, T. Tanoue, T. Shima, A. Imaoka, T. Kuwahara, Y. Momose, G. Cheng, S. Yamasaki, T. Saito, Y. Ohba, T. Taniguchi, K. Takeda, S. Hori, I. I. Ivanov, Y. Umesaki, K. Itoh, K. Honda, Induction of colonic regulatory T cells by indigenous Clostridium species. *Science* **331**, 337–341 (2011).

33. K. Suzuki, M. Maruya, S. Kawamoto, K. Sitnik, H. Kitamura, W. W. Agace, S. Fagarasan, The sensing of environmental stimuli by follicular dendritic cells promotes immunoglobulin A generation in the gut. *Immunity* **33**, 71–83 (2010).

34. A. Cerutti, The regulation of IgA class switching. *Nat. Rev. Immunol.* **8**, 421–434 (2008).

35. A. R. Albright, J. Kabat, M. Li, F. Raso, A. Reboldi, J. R. Muppidi, TGFβ signaling in germinal center B cells promotes the transition from light zone to dark zone. *J Exp Med* **216**, 2531–2545 (2019).

36. S. Casola, K. L. Otipoby, M. Alimzhanov, S. Humme, N. Uyttersprot, J. L. Kutok, M. C. Carroll, K. Rajewsky, B cell receptor signal strength determines B cell fate. *Nat. Immunol.* **5**, 317–327 (2004).

37. W. Shao, Y. Wang, Q. Fang, W. Shi, H. Qi, Epigenetic recording of stimulation history reveals BLIMP1-BACH2 balance in determining memory B cell fate upon recall challenge. *Nat. Immunol.* **25**, 1432–1444 (2024).

38. S. T. Chen, T. Y. Oliveira, A. Gazumyan, M. Cipolla, M. C. Nussenzweig, B cell receptor signaling in germinal centers prolongs survival and primes B cells for selection. *Immunity* **56**, 547–561.e7 (2023).

39. F. Raso, S. Liu, M. J. Simpson, G. M. Barton, C. T. Mayer, M. Acharya, J. R. Muppidi, A. Marshak-Rothstein, A. Reboldi, Antigen receptor signaling and cell death resistance controls intestinal humoral response zonation. *Immunity* **56**, 2373–2387.e8 (2023).

40. C. Sundling, A. W. Y. Lau, K. Bourne, C. Young, C. Laurianto, J. R. Hermes, R. J. Menzies, D. Butt, N. J. Kräutler, D. Zahra, D. Suan, R. Brink, Positive selection of IgG over IgM B cells in the germinal center reaction. *Immunity* **54**, 988–1001.e5 (2021).

41. N. Engels, L. M. König, C. Heemann, J. Lutz, T. Tsubata, S. Griep, V. Schrader, J. Wienands, Recruitment of the cytoplasmic adaptor Grb2 to surface IgG and IgE provides antigen receptor-intrinsic costimulation to class-switched B cells. *Nat. Immunol.* **10**, 1018–1025 (2009).

42. W. Liu, E. Chen, X. W. Zhao, Z. P. Wan, Y. R. Gao, A. Davey, E. Huang, L. Zhang, J. Crocetti, G. Sandoval, M. G. Joyce, C. Miceli, J. Lukszo, L. Aravind, W. Swat, J. Brzostowski, S. K. Pierce, The scaffolding protein synapse-associated protein 97 is required for enhanced signaling through isotype-switched IgG memory B cell receptors. *Sci. Signal.* **5**, ra54 (2012).

43. T.-C. Cheong, M. Compagno, R. Chiarle, Editing of mouse and human immunoglobulin genes by CRISPR-Cas9 system. *Nat. Commun.* **7**, 10934 (2016).

44. O. Talay, D. Yan, H. D. Brightbill, E. E. M. Straney, M. Zhou, E. Ladi, W. P. Lee, J. G. Egen, C. D. Austin, M. Xu, L. C. Wu, IgE^+ memory B cells and plasma cells generated through a germinal-center pathway. *Nat. Immunol.* **13**, 396–404 (2012).

45. T. Inoue, Y. Matsumoto, C. Kawai, M. Ito, S. Nada, M. Okada, T. Kurosaki, Csk restrains BCR-mediated ROS production and contributes to germinal center selection and affinity maturation. *J. Exp. Med.* **221** (2024).

46. J. C. Yam-Puc, L. Zhang, R. A. Maqueda-Alfaro, L. Garcia-Ibanez, Y. Zhang, J. Davies, Y. A. Senis, M. Snaith, K.-M. Toellner, Enhanced BCR signaling inflicts early plasmablast and germinal center B cell death. *iScience* **24**, 102038 (2021).

47. A. J. MacLean, N. Richmond, L. Koneva, M. Attar, C. A. P. Medina, E. E. Thornton, A. C. Gomes, A. El-Turabi, M. F. Bachmann, P. Rijal, T. K. Tan, A. Townsend, S. N. Sansom, O. Bannard, T. I. Arnon, Secondary influenza challenge triggers resident memory B cell migration and rapid relocation to boost antibody secretion at infected sites. *Immunity* **55**, 718–733.e8 (2022).

48. A. J. MacLean, J. P. P. L. Bonifacio, S. L. Oram, M. O. Mohsen, M. F. Bachmann, T. I. Arnon, Regulation of pulmonary plasma cell responses during secondary infection with influenza virus. *J Exp Med* **221** (2024).

49. R. Gailleton, N. R. Mathew, L. Reusch, K. Schön, L. Scharf, A. Strömberg, A. Cvjetkovic, L. Aziz, J. Hellgren, K.-W. Tang, M. Bemark, D. Angeletti, Ectopic germinal centers in the nasal turbinates contribute to B cell immunity to intranasal viral infection and vaccination. *Proc Natl Acad Sci U S A* **122**, e2421724122 (2025).

50. S. Ceglia, A. Berthelette, K. Howley, Y. Li, B. Mortzfeld, S. K. Bhattarai, N. K. H. Yiew, Y. Xu, R. Brink, J. G. Cyster, L. V. Hooper, G. J. Randolph, V. Bucci, A. Reboldi, An epithelial cell-derived metabolite tunes immunoglobulin A secretion by gut-resident plasma cells. *Nat Immunol* **24**, 531–544 (2023).

51. L. B. Rodda, P. A. Morawski, K. B. Pruner, M. L. Fahning, C. A. Howard, N. Franko, J. Logue, J. Eggenberger, C. Stokes, I. Golez, M. Hale, M. Gale Jr, H. Y. Chu, D. J. Campbell, M. Pepper, Imprinted SARS-CoV-2-specific memory lymphocytes define hybrid immunity. *Cell* **185**, 1588–1601.e14 (2022).

52. T. Hand, Y. Belkaid, Microbial control of regulatory and effector T cell responses in the gut. *Curr. Opin. Immunol.* **22**, 63–72 (2010).

53. W. Luo, L. Conter, R. A. Elsner, S. Smita, F. Weisel, D. Callahan, S. Wu, M. Chikina, M. Shlomchik, IL-21R signal reprogramming cooperates with CD40 and BCR signals to select and differentiate germinal center B cells. *Sci. Immunol.* **8**, eadd1823 (2023).

54. L. Zhang, A. Toboso-Navasa, A. Gunawan, A. Camara, R. Nakagawa, K. Finsterbusch, P. Chakravarty, R. Newman, Y. Zhang, M. Eilers, A. Wack, P. Tolar, K.-M. Toellner, D. P. Calado, Regulation of BCR-mediated Ca mobilization by MIZ1-TMBIM4 safeguards IgG1 GC B cell-positive selection. *Sci Immunol* **9**, eadk0092 (2024).

55. P. K. Mattila, C. Feest, D. Depoil, B. Treanor, B. Montaner, K. L. Otipoby, R. Carter, L. B. Justement, A. Bruckbauer, F. D. Batista, The actin and tetraspanin networks organize receptor nanoclusters to regulate B cell receptor-mediated signaling. *Immunity* **38**, 461–474 (2013).

56. J. Lee, P. Sengupta, J. Brzostowski, J. Lippincott-Schwartz, S. K. Pierce, The nanoscale spatial organization of B-cell receptors on immunoglobulin M- and G-expressing human B-cells. *Mol Biol Cell* **28**, 511–523 (2017).

57. K. Moor, M. Diard, M. E. Sellin, B. Felmy, S. Y. Wotzka, A. Toska, E. Bakkeren, M. Arnoldini, F. Bansept, A. D. Co, T. Völler, A. Minola, B. Fernandez-Rodriguez, G. Agatic, S. Barbieri, L. Piccoli, C. Casiraghi, D. Corti, A. Lanzavecchia, R. R. Regoes, C. Loverdo, R. Stocker, D. R. Brumley, W.-D. Hardt, E. Slack, High-avidity IgA protects the intestine by enchaining growing bacteria. *Nature* **544**, 498–502 (2017).

58. S. Sheikh-Mohamed, B. Isho, G. Y. C. Chao, M. Zuo, C. Cohen, Y. Lustig, G. R. Nahass, R. E. Salomon-Shulman, G. Blacker, M. Fazel-Zarandi, B. Rathod, K. Colwill, A. Jamal, Z. Li, K. Q. de Launay, A. Takaoka, J. Garnham-Takaoka, A. Patel, C. Fahim, A. Paterson, A. X. Li, N. Haq, S. Barati, L. Gilbert, K. Green, M. Mozafarihashjin, P. Samaan, P. Budylowski, W. L. Siqueira, S. Mubareka, M. Ostrowski, J. M. Rini, O. L. Rojas, I. L. Weissman, M. C. Tal, A. McGeer, G. Regev-Yochay, S. Straus, A.-C. Gingras, J. L. Gommerman, Systemic and mucosal IgA responses are variably induced in response to SARS-CoV-2 mRNA vaccination and are associated with protection against subsequent infection. *Mucosal Immunol.* **15**, 799–808 (2022).

59. C. Gregoire, L. Spinelli, S. Villazala-Merino, L. Gil, M. P. Holgado, M. Moussa, C. Dong, A. Zarubica, M. Fallet, J.-M. Navarro, B. Malissen, P. Milpied, M. Gaya, Viral infection engenders bona fide and bystander subsets of lung-resident memory B cells through a permissive mechanism. *Immunity* **55**, 1216–1233.e9 (2022).

Acknowledgements

We thank Rejane Rua, Achille Broggi and Romain Roncagalli for analysis and interpretation of confocal images and signaling experiments. We thank Myriam Baratin, Pierre Golstein and Philippe Naquet for scientific discussions and feedback on the manuscript. We thank Manon Fabregue, Solene Mathieu and Capucine Guerry for technical support. We thank Bernard Malissen and CIPHE-GEMTISConsortium investigators for the development of Igha-tdTom and Igha-Δtail-tdTom mice. We thank Claude-Agnès Reynaud and Jean Claude Weill for providing Aicda-CreERT2 mice. We thank Tasuku Honjo and Daniel Pinschewer for providing *Aid*(G23S) mice. We thank Julien Marie for providing Tgfbr2$^{fl/fl}$ mice. We thank Ronan Le Goffic for providing influenza virus strains. We thank David Holden for providing *Salmonella* sp. strains. We thank Régis Tournebize for providing *Klebsiella* sp. strains. We thank the flow cytometry and imaging (Imagimm) platforms for technical support and the biological resource unit for the breeding of animals (CIML).

Funding

This work was supported by the ERC Starting Grant (EU), ATIP-AVENIR (France) ad ANR Jeunes Chercheurs (France) to MG; the Marie Sklodowska Curie fellowship (EU) to MPH; the Centre d'Immunologie de Marseille Luminy (CIML), which receives its core funding from Aix Marseille University, CNRS and INSERM.

Author contributions: MG conceived and supervised the study. MPH, SO and MG designed the experiments. MPH, SO, LB, MM, AT, AZ, CG and MG performed the experiments. FF developed Igha-tdTom and Igha-Δtail-tdTom mice. ES, ML and MC provided materials. ES, ML, MC and CG provided discussion and edited the paper. MG, MPH and SO analyzed the data, made the figures and wrote the paper.

Competing interests: Authors declare that they have no competing interests.

Data and materials availability: All data are available in the main text or the supplementary materials.

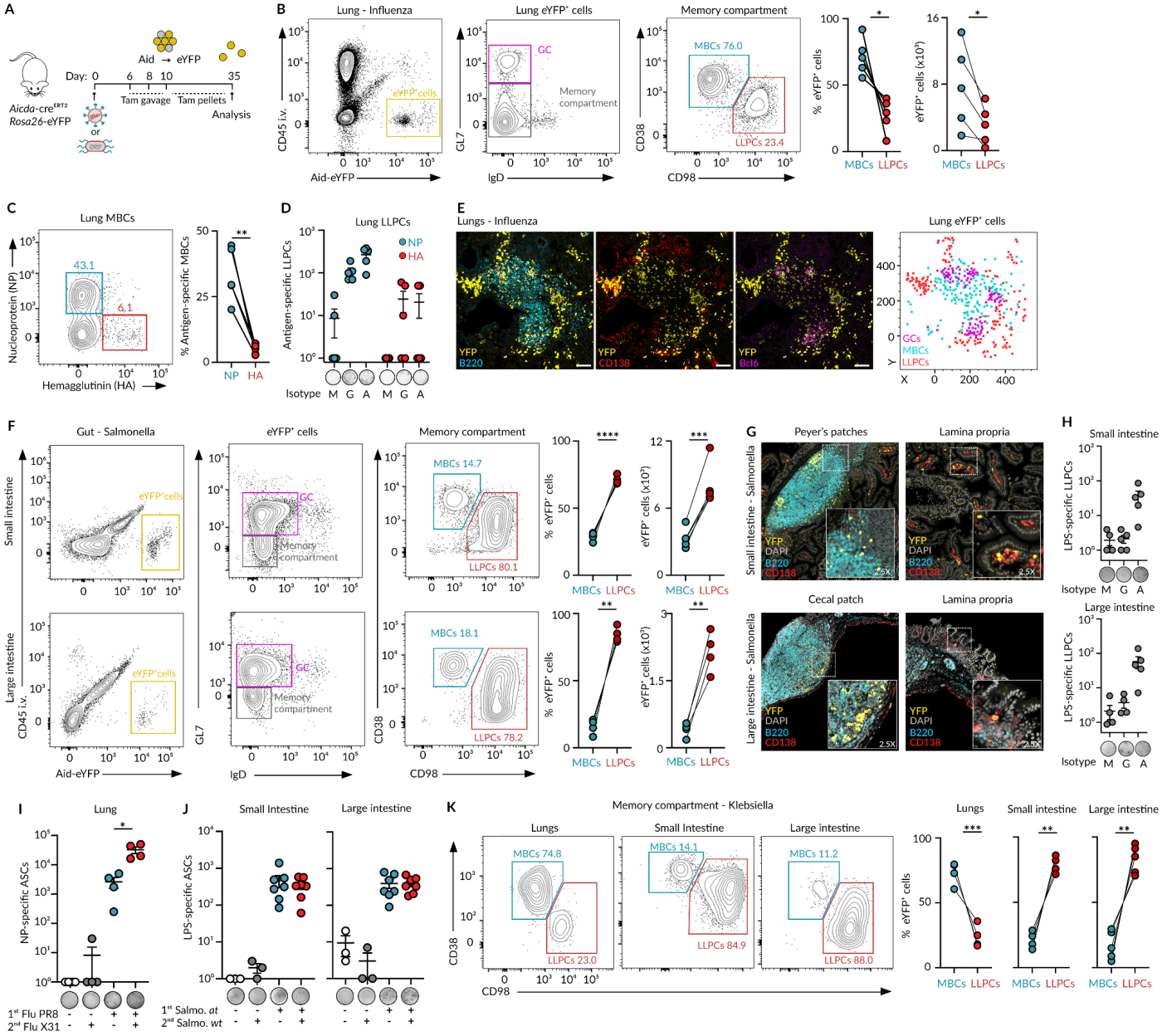

Figure 1. Mucosal infection elicits divergent B cell memory strategies in lungs and gut. (**A**) Overview of experimental approach. (**B**) Flow cytometry plots displaying the gating strategy of lung YFP$^+$ B cells, memory cells (GL7$^-$), MBCs (CD38$^+$CD98$^-$), and LLPCs (CD38^{low}CD98$^+$) in Aid-EYFP mice infected with influenza virus and treated as in (A). Quantifications indicate percentages and absolute numbers of MBCs and LLPCs. (**C**) Contour plots and quantification of lung YFP$^+$ MBCs binding to NP and HA antigens. (**D**) Enumeration of lung NP- and HA-specific IgM$^+$, IgG$^+$, and IgA$^+$ antibody-secreting cells by ELISpot. (**E**) Confocal images of lung sections stained for YFP (yellow), B220 (cyan), CD138 (red), and Bcl6 (magenta). Scale bars, 70 µm. X and Y positions of MBCs (B220$^+$Bcl6$^-$, cyan), GCs (B220$^+$Bcl6$^+$, magenta) and LLPCs (B220^{low}CD138$^+$, red). (**F**) Gating strategy of YFP$^+$ cells in the small (Peyer's patches and lamina propria) and large (cecal patch and lamina propria) intestine in Aid-EYFP animals infected with *Salmonella typhimurium* and treated as in (A). Quantifications show the percentage and absolute numbers of MBCs and LLPCs. (**G**) Confocal microscopy images of small and large intestine sections stained for YFP (yellow), B220 (cyan), CD138 (red) and DAPI (grey). (**H**) Enumeration of gut LPS-specific antibody-secreting cells by ELISpot. (**I** and **J**) Enumeration of (**I**) NP-specific or (**J**) LPS-specific antibody-secreting cells in lungs or gut

after re-challenge with influenza X-31 or *Salmonella* wild type, respectively. (**K**) Flow cytometry of MBCs and LLPCs in lungs and gut of Aid-EYFP mice following *Klebsiella pneumoniae* infection. In all panels, quantifications display one representative experiment out of three, mean ± s.e.m. Each dot represents one mouse. Paired t-test (**B**, **C**, **F, K**) and ANOVA (**I** and **J**): *p<0.05, **p<0.01, ***p<0.001 and ****p<0.0001.

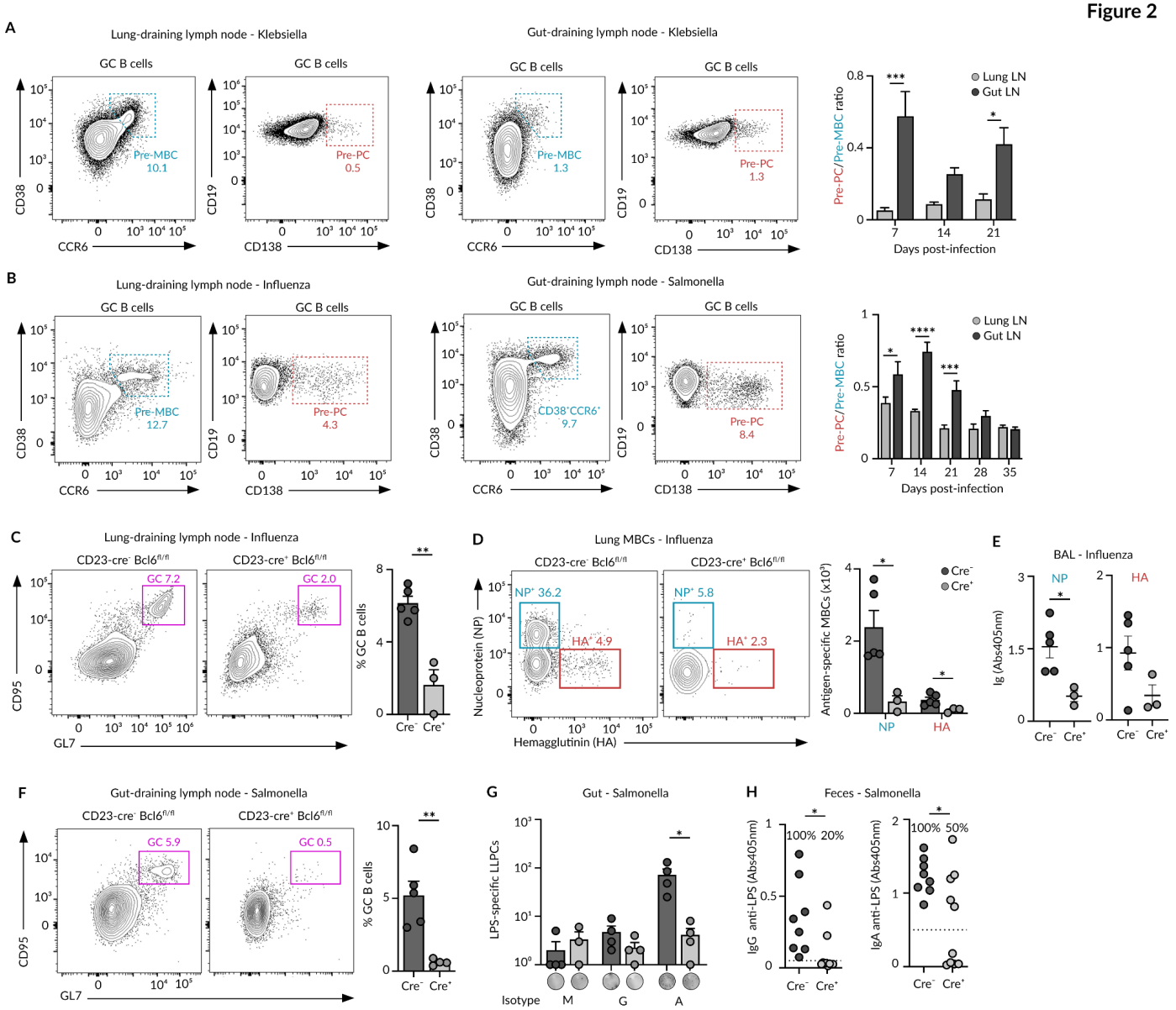

Figure 2. Differential selection in GC reactions shape mucosal memory compartments. (**A** and **B**) Flow cytometry plots and quantification of pre-MBCs ($CD38^+CCR6^+$) and pre-PCs ($CD138^+$) within the GC reaction ($CD95^+GL7^+$) in lung and gut draining lymph nodes after (A) Klebsiella or (B) Influenza/Salmonella infection. (**C**) Flow cytometry plots and quantification of GC B cells in lung-draining lymph nodes of CD23-cre $Bcl6^{fl/fl}$ mice infected with influenza virus (day 35). (**D**) Contour plots and quantification of lung MBCs binding to fluorescently-labeled NP and HA antigens. (**E**) Quantification of NP and HA-specific immunoglobulin levels in the bronchoalveolar fluid. (**F**) Flow cytometry plots and quantification of GC B cells in gut-draining lymph nodes of CD23-cre $Bcl6^{fl/fl}$ mice infected with Salmonella (day 35). (**G**) Enumeration of gut LPS-specific IgM^+, IgG^+, and IgA^+ antibody-secreting cells by ELISpot. (**H**) Quantification of LPS-specific immunoglobulin levels in fecal extracts. Percentage of responders is shown. All panels display quantification from one representative experiment out of three (mean ± s.e.m.). Each dot represents one mouse. t-test (**A**-**H**): *p<0.05, **p<0.01, ***p<0.001 and ****p<0.0001.

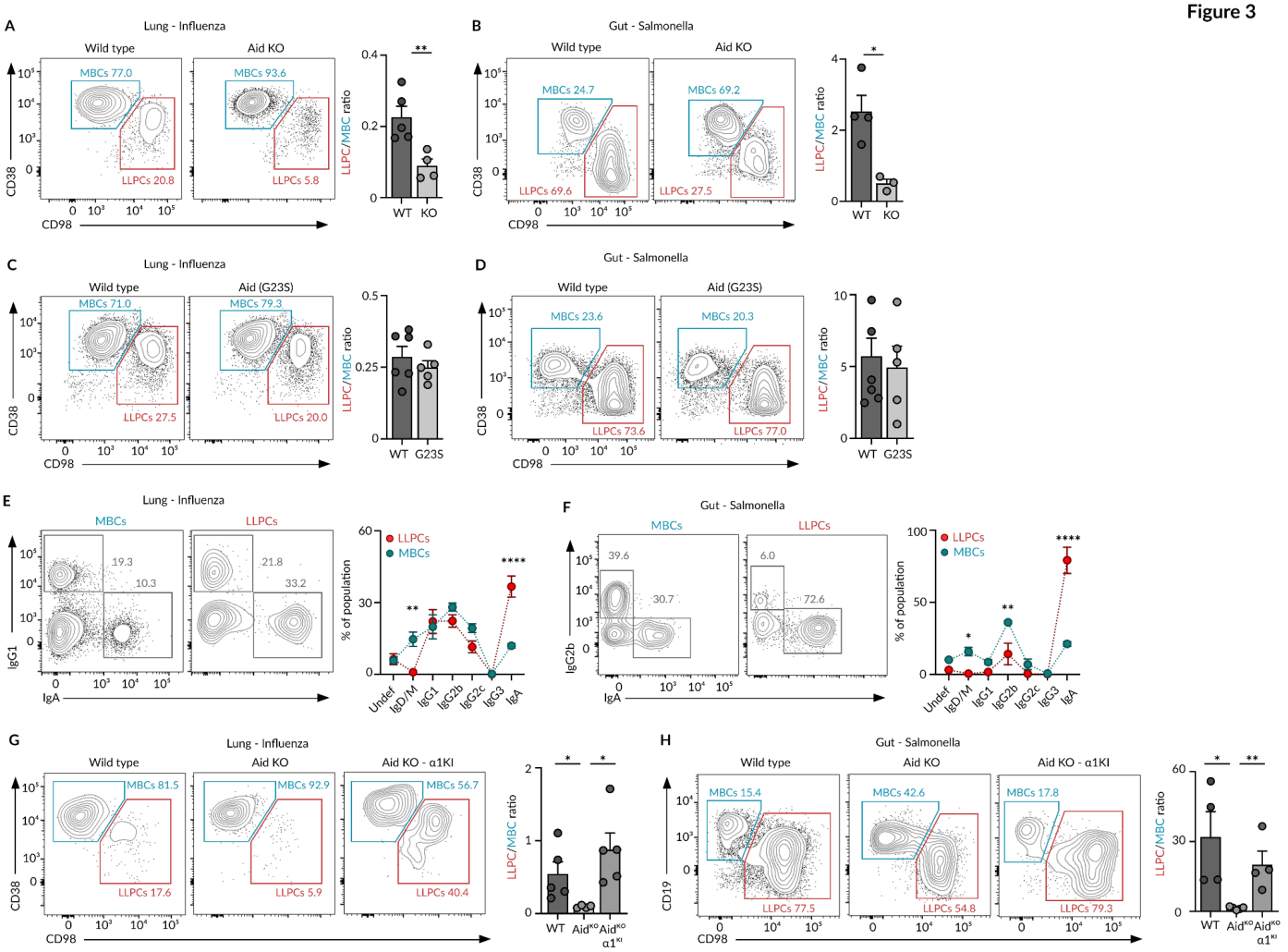

Figure 3. Mucosal memory selection relies on IgA BCR expression rather than affinity. (**A** and **B**) Flow cytometry plots display MBC ($CD38^{+}CD98^{-}$) and LLPC ($CD38^{low}CD98^{+}$) distribution in (A) lungs of influenza-infected and (B) gut of *Salmonella*-infected wild type and *Aid*-KO mice. Bar charts show LLPC:MBC ratios. (**C** and **D**) Flow cytometry plots display MBC and LLPC distribution in (C) lungs of influenza-infected and (D) gut of *Salmonella*-infected wild type and *Aid*(G23S) mice. Bar charts show LLPC:MBC ratios. (**E** and **F**) Contour plots and quantification of isotype distribution within MBCs and LLPCs in (E) lungs of influenza-infected mice and (F) gut of *Salmonella*-infected mice. (**G** and **H**) Flow cytometry plots displaying MBC versus LLPC distribution in (G) lungs of influenza-infected and (H) gut of *Salmonella*-infected wild type, *Aid*-KO and *Aid*-KO-αKI mice. Bar charts show LLPC:MBC ratios. All panels display quantification from one representative experiment out of three (mean ± s.e.m.). Each dot represents one mouse. t-test (**A**-**D**) and one-way ANOVA (**E**-**H**): *p<0.05, **p<0.01 and ****p<0.0001.

Figure 4

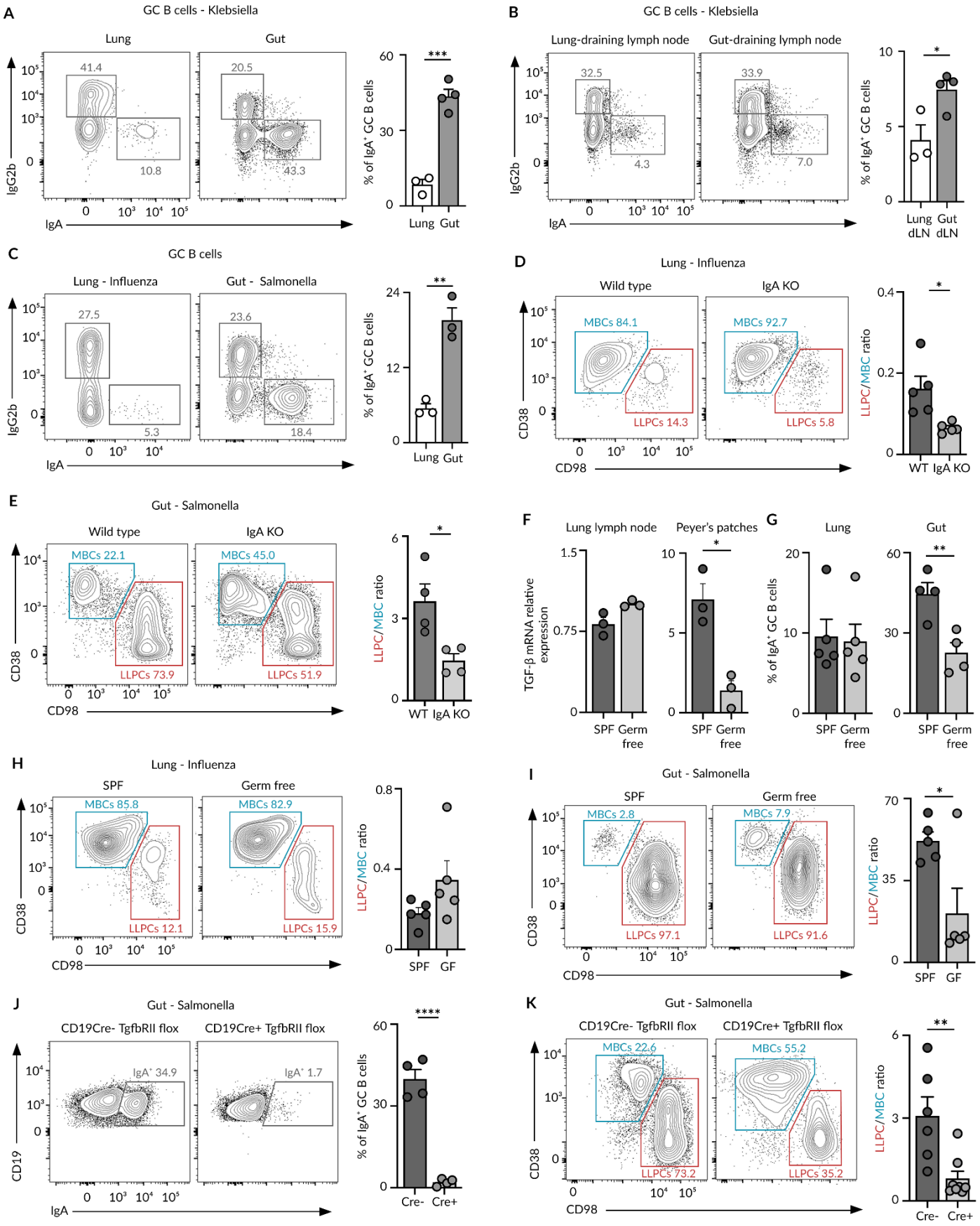
A
GC B cells - Klebsiella
Lung
Gut
41.4
10.8
20.5
43.3
IgG2b
IgA
% of IgA+ GC B cells
***
Lung Gut
B
GC B cells - Klebsiella
Lung-draining lymph node
Gut-draining lymph node
32.5
4.3
33.9
7.0
*
Lung dLN
Gut dLN
C
GC B cells
Lung - Influenza
Gut - Salmonella
27.5
5.3
23.6
18.4
**
D
Lung - Influenza
Wild type
IgA KO
MBCs 84.1
LLPCs 14.3
MBCs 92.7
LLPCs 5.8
CD38
CD98
LLPC/MBC ratio
WT IgA KO
E
Gut - Salmonella
Wild type
IgA KO
MBCs 22.1
LLPCs 73.9
MBCs 45.0
LLPCs 51.9
F
Lung lymph node
Peyer's patches
TGF-β mRNA relative expression
SPF Germ free
G
Lung
Gut
H
Lung - Influenza
SPF
Germ free
MBCs 85.8
LLPCs 12.1
MBCs 82.9
LLPCs 15.9
SPF GF
I
Gut - Salmonella
MBCs 2.8
LLPCs 97.1
MBCs 7.9
LLPCs 91.6
J
Gut - Salmonella
CD19Cre- TgfbRII flox
CD19Cre+ TgfbRII flox
IgA+ 34.9
IgA+ 1.7
CD19
****
Cre- Cre+
K
Gut - Salmonella
MBCs 22.6
LLPCs 73.2
MBCs 55.2
LLPCs 35.2

Figure 4. The intestinal microbiota favors the TGFβ-IgA-LLPC axis. (**A**-**B**) Flow cytometry plots and quantification of IgA BCR isotype usage within the GC population in (A) lungs and gut or (B) draining lymph nodes after *Klebsiella* infection (day 14). (**C**) Flow cytometry plots and quantification of IgA BCR isotype usage within the GC population in lungs and gut after influenza or *Salmonella* infection (day 14). (**D** and **E**) Contour plots and quantification of MBCs and LLPCs in (D) lungs and (E) gut of wild type and *Igha*-KO mice infected with influenza virus or *Salmonella*, respectively. Bar charts represent the LLPC:MBC ratio. (**F**) Quantification of TGFβ mRNA levels in lung lymph nodes and Peyer's patches of SPF and Germ free mice by qPCR. Cytokine expression was normalized to β-actin. (**G**) Quantification of IgA expression by GC B cells in lungs and gut of influenza or Salmonella-infected mice (**H** and **I**) Contour plots and quantification of MBCs and LLPCs in (H) lungs and (I) gut of SPF and Germ free mice infected with influenza virus or Salmonella. Bar charts represent the LLPC:MBC ratio. (**J**) Flow cytometry plots and quantification displaying IgA expression by GC B cells in the gut of *Salmonella*-infected CD19-cre Tgfbr2$^{fl/fl}$ mice. (**K**) Contour plots and quantification of MBCs and LLPCs in the gut of CD19-cre Tgfbr2$^{fl/fl}$ mice infected with *Salmonella*. Bar charts represent the LLPC:MBC ratio. In all panels, bar charts show the quantification of one representative experiment out of three, mean ± s.e.m. Each dot represents one mouse. t test (**A**-**K**): *p<0.05, **p<0.01, ***p<0.001 and ****p<0.0001.

Figure 5

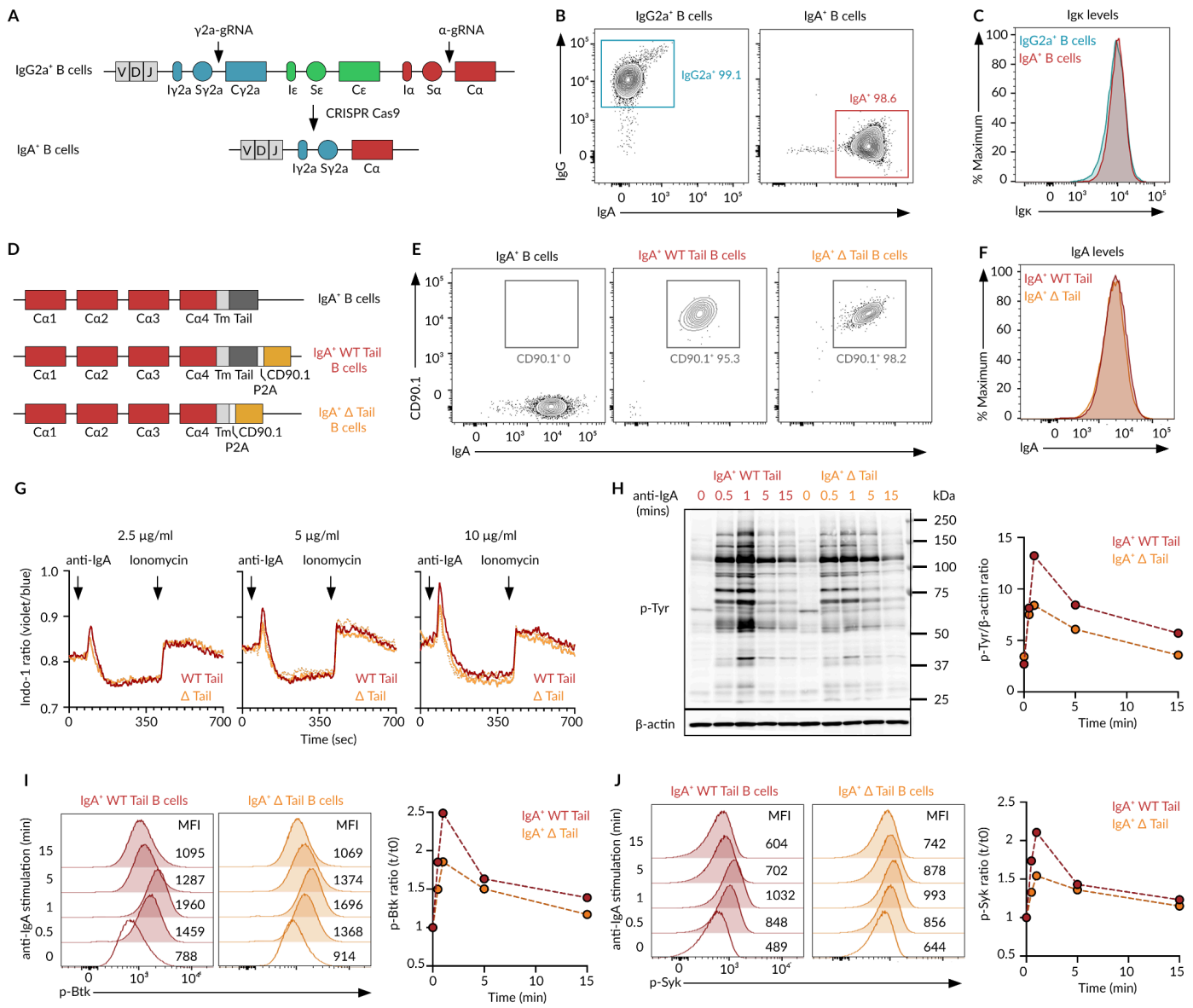

Figure 5. The IgA BCR requires its cytosolic tail for efficient signal transduction. (**A**) Schematic representation of the strategy used to force class-switching of A20 B cells from IgG2a to IgA with CRISPR/Cas9. (**B**) Contour plots show IgG2a versus IgA expression 21 days after transfection and clonal dilution of cells engineered as in (A). (**C**) Histogram shows Kappa light chain levels in IgG2a⁺ and IgA⁺ A20 B cells. (**D**) Schematic strategy used to remove the cytosolic tail from IgA⁺ A20 B cells. (**E**) Contour plots show the expression of IgA BCR and CD90.1 in WT and Δtail A20 B cells generated in (D). (**F**) Histogram shows similar IgA BCR surface levels in WT and Δtail A20 B cells. (**G**) Ca^{2+} mobilization in IgA⁺ WT (red) and IgA⁺ Δtail (orange) A20 B cells stimulated with increasing concentrations of anti-mouse IgA and ionomycin at indicated time points. Full and dotted lines represent different clones. (**H**) Immunoblot analysis and quantification of lysates from IgA⁺ WT (red) and IgA⁺ Δtail (orange) A20 B cells, either untreated or stimulated for various times with anti-IgA. Membranes were probed with anti-phosphotyrosine (top) and anti-β-actin (bottom). (**I** and **J**) Phospho-flow cytometry histograms and quantification of (I) Btk and (J) Syk MFI in IgA⁺ WT (red) and IgA⁺ Δtail (orange) B cells after stimulation with anti-mouse IgA. MFI values were relativized to time=0.

Figure 6

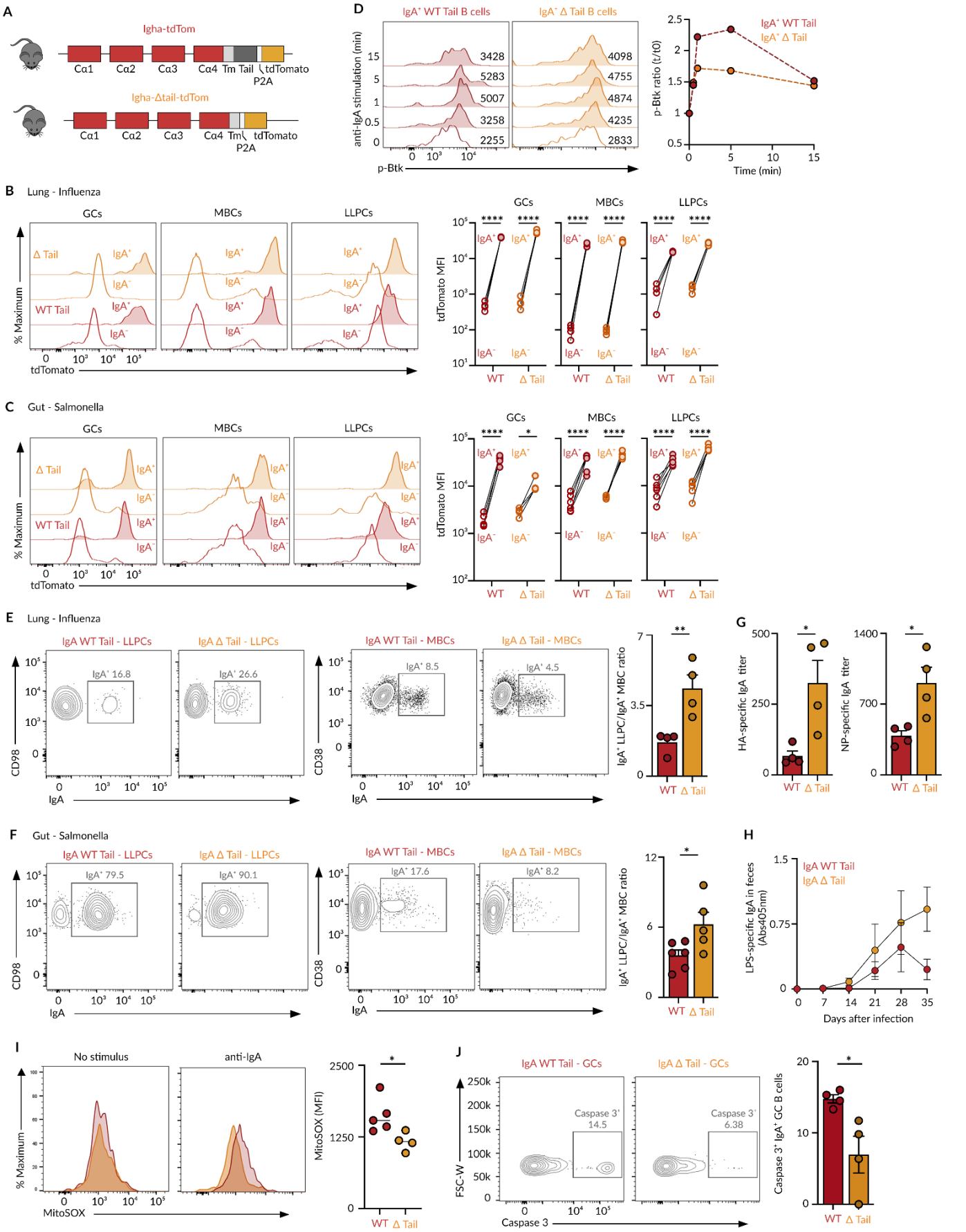
A
Igha-tdTom
Cα1 Cα2 Cα3 Cα4 Tm Tail tdTomato
P2A
Igha-Δtail-tdTom
Cα1 Cα2 Cα3 Cα4 Tm tdTomato
P2A
D
IgA+ WT Tail B cells
IgA+ Δ Tail B cells
anti-IgA stimulation (min)
p-Btk
p-Btk ratio (t/t0)
Time (min)
IgA+ WT Tail
IgA+ Δ Tail
B Lung - Influenza
GCs
MBCs
LLPCs
Δ Tail
WT Tail
% Maximum
tdTomato
tdTomato MFI
WT
Δ Tail
C Gut - Salmonella
E Lung - Influenza
IgA WT Tail - LLPCs
IgA Δ Tail - LLPCs
IgA WT Tail - MBCs
IgA Δ Tail - MBCs
CD98
CD38
IgA
IgA+ LLPC/IgA+ MBC ratio
G
HA-specific IgA titer
NP-specific IgA titer
F Gut - Salmonella
H
LPS-specific IgA in feces (Abs405nm)
Days after infection
I
No stimulus
anti-IgA
MitoSOX
MitoSOX (MFI)
J
IgA WT Tail - GCs
IgA Δ Tail - GCs
Caspase 3
FSC-W
Caspase 3+ IgA+ GC B cells

Figure 6. The IgA cytosolic tail balances LLPC entry by modulating BCR signaling. (**A**) Schematic representation of Igha-tdTom and Igha-Δtail-tdTom mouse lines. (**B** and **C**) Histograms and quantifications show the expression of tdTomato in IgA^- or IgA^+ GCs, MBCs and LLPCs in (**B**) lungs of influenza-infected and (**C**) gut of Salmonella-infected Igha-tdTom and Igha-Δtail-tdTom mice. (**D**) Phospho-flow cytometry histograms and quantification of Btk MFI in IgA^+ WT (red) and IgA^+ Δtail (orange) B cells from Peyer's patches after stimulation with anti-mouse IgA. MFI values were relativized to time=0. (**E** and **F**) Contour plots displaying IgA^+ cells within MBC and LLPC populations in (**E**) lungs and (**F**) gut of Igha-tdTom and Igha-Δtail-tdTom mice infected with influenza virus or *Salmonella*, respectively. Quantifications show IgA^+ LLPC: IgA^+ MBC ratios. (**G** and **H**) Quantification of (G) HA- and NP- specific IgA antibody levels in the blood after Influenza infection and (H) LPS-specific IgA antibodies in the feces after Salmonella infection. **(I)** Flow cytometry histograms and quantification of MitoSOX fluorescence in IgA^+ WT (red) and IgA^+ Δtail (orange) GC B cells incubated with or without anti-IgA. **(J)** Flow cytometry analysis and quantification of Caspase-3 staining in IgA^+ WT (red) and IgA^+ Δtail (orange) GC B cells. All panels display quantification from one representative experiment out of three (mean ± s.e.m.). Each dot represents one mouse. 2-way ANOVA (**B** and **C**) and t test (**E-J**): *$p<0.05$, **$p<0.01$ and ****$p<0.0001$.

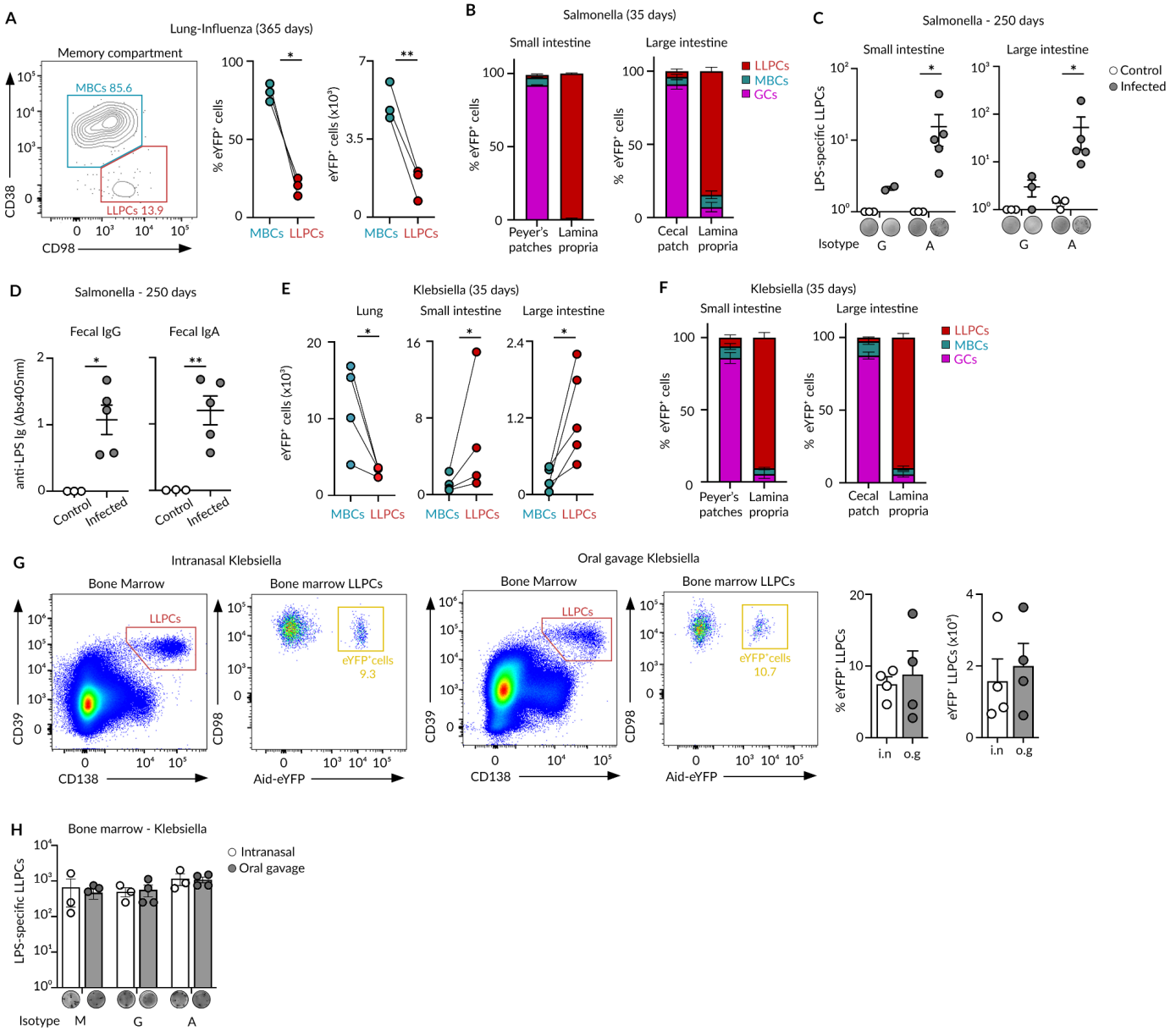

Figure S1. Long-term maintenance of mucosal B cell memory compartments. (**A**) Flow cytometry plots displaying MBCs and LLPCs in lungs of Aid-EYFP mice 365 days post infection with influenza virus. Quantifications indicate percentages and absolute numbers of MBCs and LLPCs. (**B**) Bar charts depict the distribution of GC, MBC and LLPC populations in the small (Peyer's patches and lamina propria) and large (cecal patch and lamina propria) intestine of Aid-EYFP mice infected with *Salmonella* (day 35). (**C**) LPS-specific antibody-secreting cells in the small and large intestine 250 days after *Salmonella* infection. (**D**) Quantification of LPS-specific immunoglobulin levels in fecal extracts 250 days after *Salmonella* infection. (**E**) Quantifications show MBC and LLPC numbers in the lungs, small and large intestines of Aid-EYFP mice 35 days post infection with *Klebsiella* (intranasally or orally). (**F**) Bar charts depict the distribution of GC, MBC and LLPC populations in the small and large intestine in Aid-EYFP animals infected with *Klebsiella* (day 35). (**G**) Flow cytometry plots display YFP$^+$ LLPCs in the bone marrow of Aid-EYFP mice infected with *Klebsiella* intranasally or orally (day 35). Bar charts show the quantification in percentage and cell numbers. (**H**) Enumeration of LPS-specific antibody-secreting cells in the bone marrow 35 days after *Klebsiella* infection intranasally or orally. In all panels, quantifications display one representative experiment, mean ± s.e.m. Each dot represents one mouse, t-test (**A**-**H**): *p<0.05 and **p<0.01.

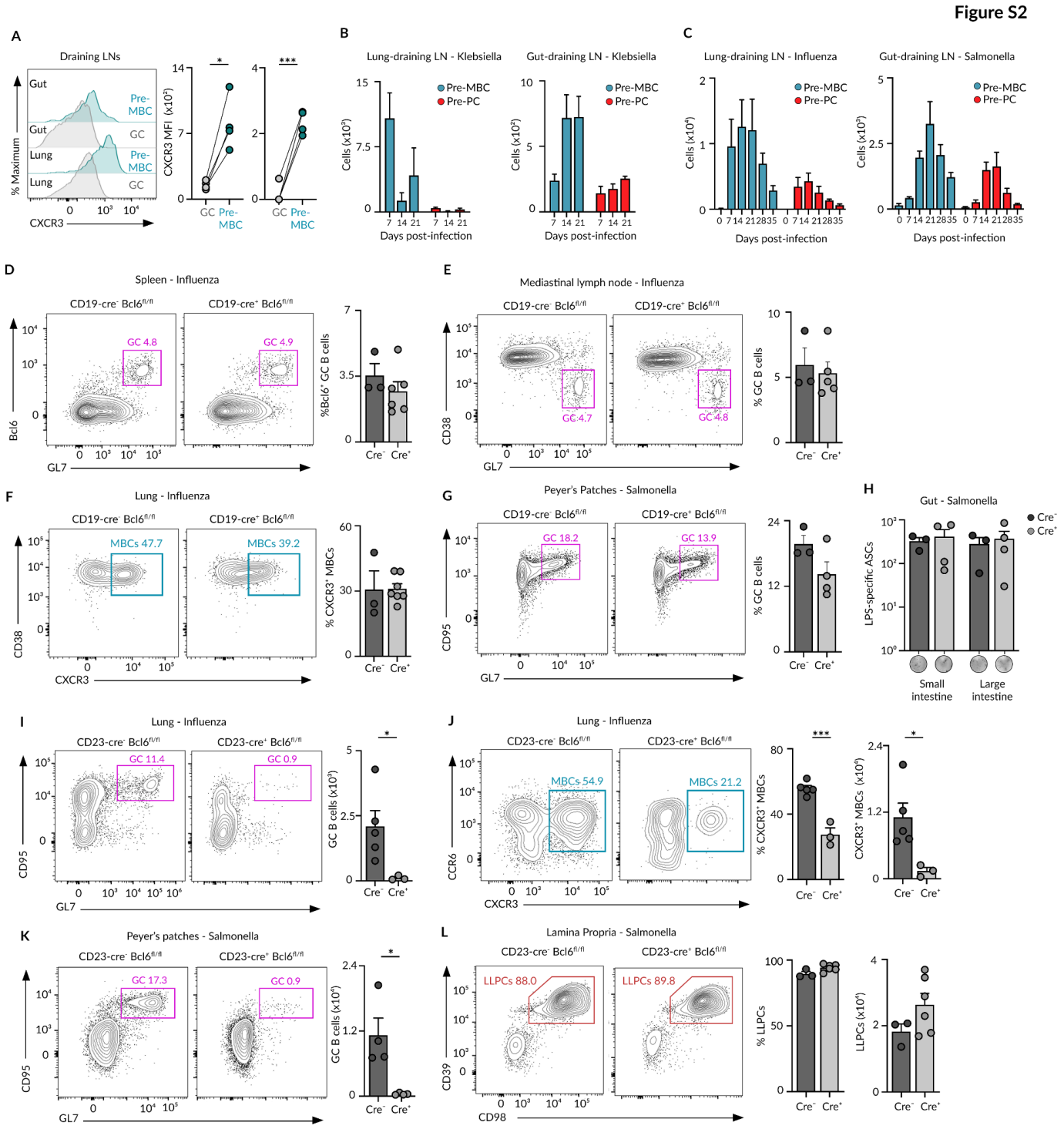

Figure S2. GC selection shapes mucosal memory compartments. (**A**) Histograms show CXCR3 expression by GCs and pre-MBCs in lung and gut draining lymph nodes after Klebsiella infection. Quantifications show CXCR3 MFI. (**B-C**) pre-MBC and pre-PC absolute numbers in lung and gut-draining lymph nodes following (B) *Klebsiella* or (C) Influenza / *Salmonella* infection. (**D**) Contour plots and quantification of Bcl6-expressing GC B cells in the spleen of CD19-cre Bcl6$^{fl/fl}$ mice after influenza infection. (**E**) Contour plots and quantification of GC B cells (CD38^{-}GL7^{+}) in mediastinal lymph nodes of CD19-cre Bcl6$^{fl/fl}$ mice after influenza infection. (**F**) Contour plots and quantification of CXCR3^{+} MBCs in the lungs of CD19-cre Bcl6$^{fl/fl}$ mice after influenza infection. (**G**) Contour plots and quantification of GC B cells (CD95^{+}GL7^{+}) in Peyer's patches of CD19-cre Bcl6$^{fl/fl}$ mice after Salmonella infection. (**H**) Enumeration of LPS-specific antibody-secreting cells measured by ELISpot in the small and large intestine of CD19-cre-Bcl6$^{fl/fl}$ mice infected with *Salmonella*. (**I**) Contour plots and quantification of GC B cells

(Fas^+GL7^+) in lungs of CD23-cre $Bcl6^{fl/fl}$ mice after influenza infection. (**J**) Contour plots and quantification of $CXCR3^+$ MBCs in the lungs of CD23-cre $Bcl6^{fl/fl}$ mice after influenza infection. (**K**) Contour plots and quantification of GC B cells (Fas^+GL7^+) in Peyer's patches of CD23-cre $Bcl6^{fl/fl}$ mice after *Salmonella* infection. (**L**) Contour plots and quantification of LLPCs in the gut of CD23-cre $Bcl6^{fl/fl}$ mice after *Salmonella* infection. In all panels, quantifications display one representative experiment, mean ± s.e.m. Each dot represents one mouse, t-test (**A**-**L**): *$p<0.05$ and ***$p<0.001$.

Figure S3

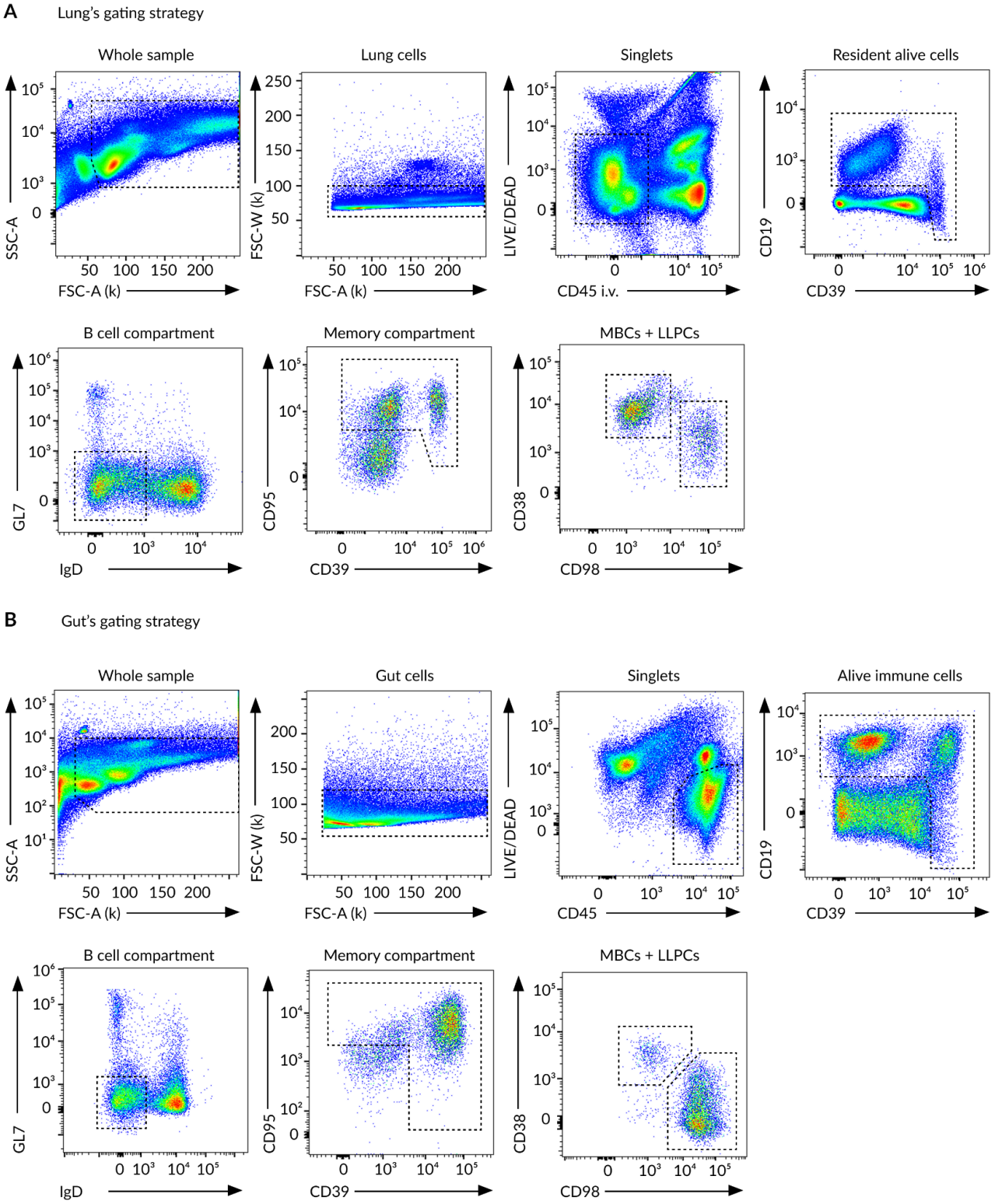

Figure S3. Gating strategy used to identify MBCs and LLPCs in non Aid-EYFP mice. (**A** and **B**) Flow cytometry plots showing the gating strategy for MBCs and LLPCs in (**A**) lungs and (**B**) gut after infection.

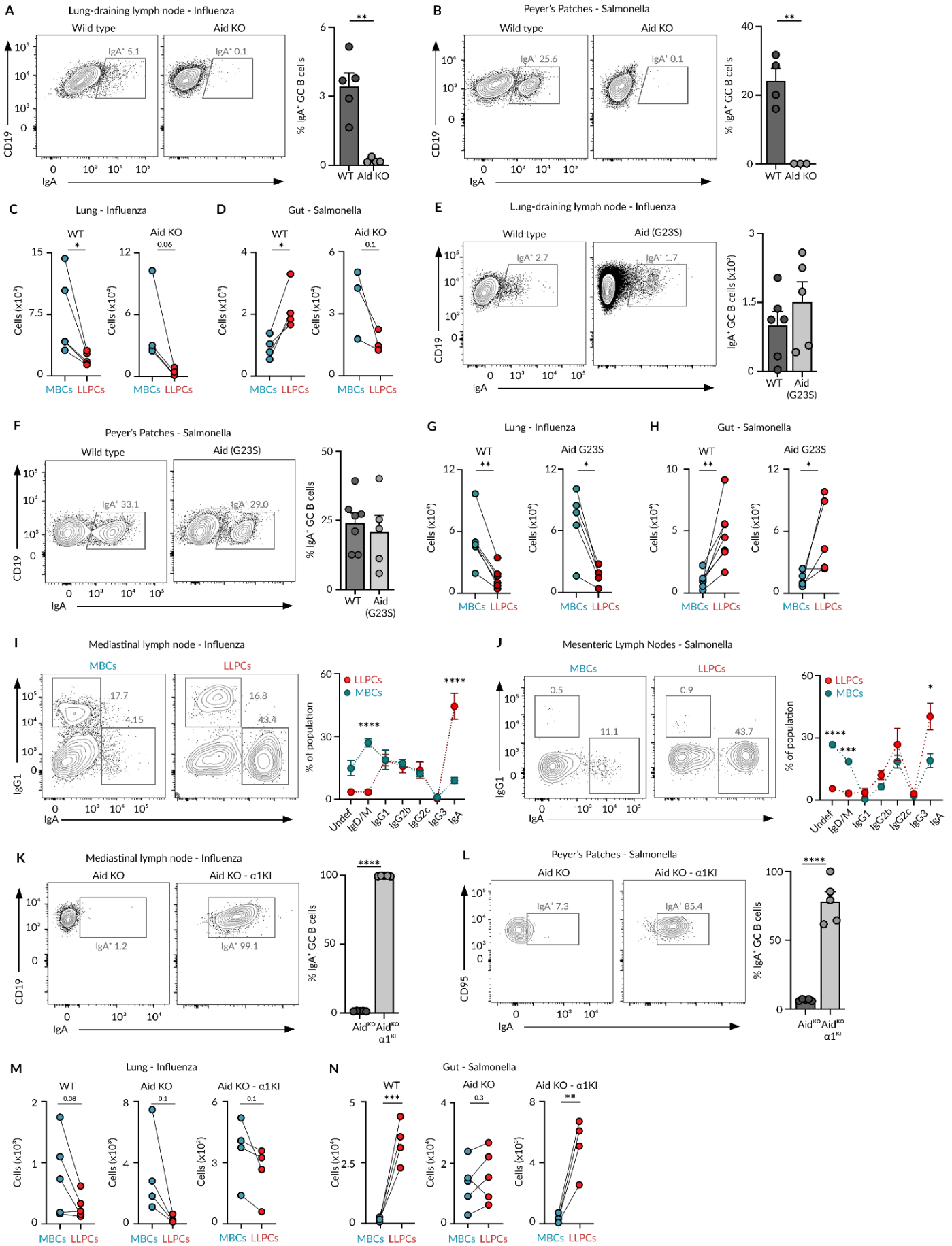
A
Lung-draining lymph node - Influenza
Wild type
Aid KO
IgA+ 5.1
IgA+ 0.1
CD19
IgA
% IgA+ GC B cells
WT Aid KO
B
Peyer's Patches - Salmonella
Wild type
Aid KO
IgA+ 25.6
IgA+ 0.1
C
Lung - Influenza
WT
Aid KO
Cells (x10³)
Cells (x10⁴)
MBCs LLPCs
D
Gut - Salmonella
E
Lung-draining lymph node - Influenza
Wild type
Aid (G23S)
IgA+ 2.7
IgA+ 1.7
IgA+ GC B cells (x10³)
F
Peyer's Patches - Salmonella
IgA+ 33.1
IgA+ 29.0
G
Lung - Influenza
Aid G23S
H
Gut - Salmonella
I
Mediastinal lymph node - Influenza
MBCs
LLPCs
IgG1
% of population
Undef IgD/M IgG1 IgG2b IgG2c IgG3 IgA
J
Mesenteric Lymph Nodes - Salmonella
K
Mediastinal lymph node - Influenza
Aid KO - α1KI
IgA+ 1.2
IgA+ 99.1
L
Peyer's Patches - Salmonella
CD95
IgA+ 7.3
IgA+ 85.4
M
Lung - Influenza
N
Gut - Salmonella

Figure S4. Dynamics of IgA BCR expression in mucosal tissues. (**A**-**B**) Flow cytometry plots display IgA expression by GC B cells in (**A**) mediastinal lymph nodes of influenza-infected and (**B**) Peyer's patches of *Salmonella*-infected wild type and *Aid* KO mice. Bar charts show the percentage of IgA$^+$ B cells in the GC population. (**C**-**D**) Quantification of MBC and LLPC numbers in (C) lungs of influenza-infected and (D) gut of *Salmonella*-infected wild type and *Aid*-KO mice (day 35). (**E**-**F**) Flow cytometry plots display IgA expression by GC B cells in (**E**) mediastinal lymph nodes of influenza-infected and (**F**) Peyer's patches of *Salmonella*-infected wild type and *Aid* (G23S) mice. (**G**-**H**) Quantification of MBC and LLPC numbers in (G) lungs of influenza-infected and (H) gut of *Salmonella*-infected wild type and *Aid* (G23S) mice (day 35). (**I**-**J**) Contour plots and quantification of isotype distribution within MBCs and LLPCs in (I) lung-draining lymph nodes of influenza-infected mice and (J) gut-draining lymph nodes of *Salmonella*-infected mice (day 35). (**K**-**L**) Flow cytometry plots display IgA expression by GC B cells in (**K**) mediastinal lymph nodes of influenza-infected and (**L**) Peyer's patches of *Salmonella*-infected wild type, *Aid* KO and *Aid* KO-α1 KI mice. (**M**-**N**) Quantification of MBC and LLPC numbers in (M) lungs of influenza-infected and (N) gut of *Salmonella*-infected wild type, *Aid* KO and *Aid* KO-α1 KI mice (day 35). In all panels, quantifications display one representative experiment, mean ± s.e.m. Each dot represents one mouse. t test: *$p<0.05$, **$p<0.01$, ***$p<0.001$ and ****$p<0.0001$.

Figure S5

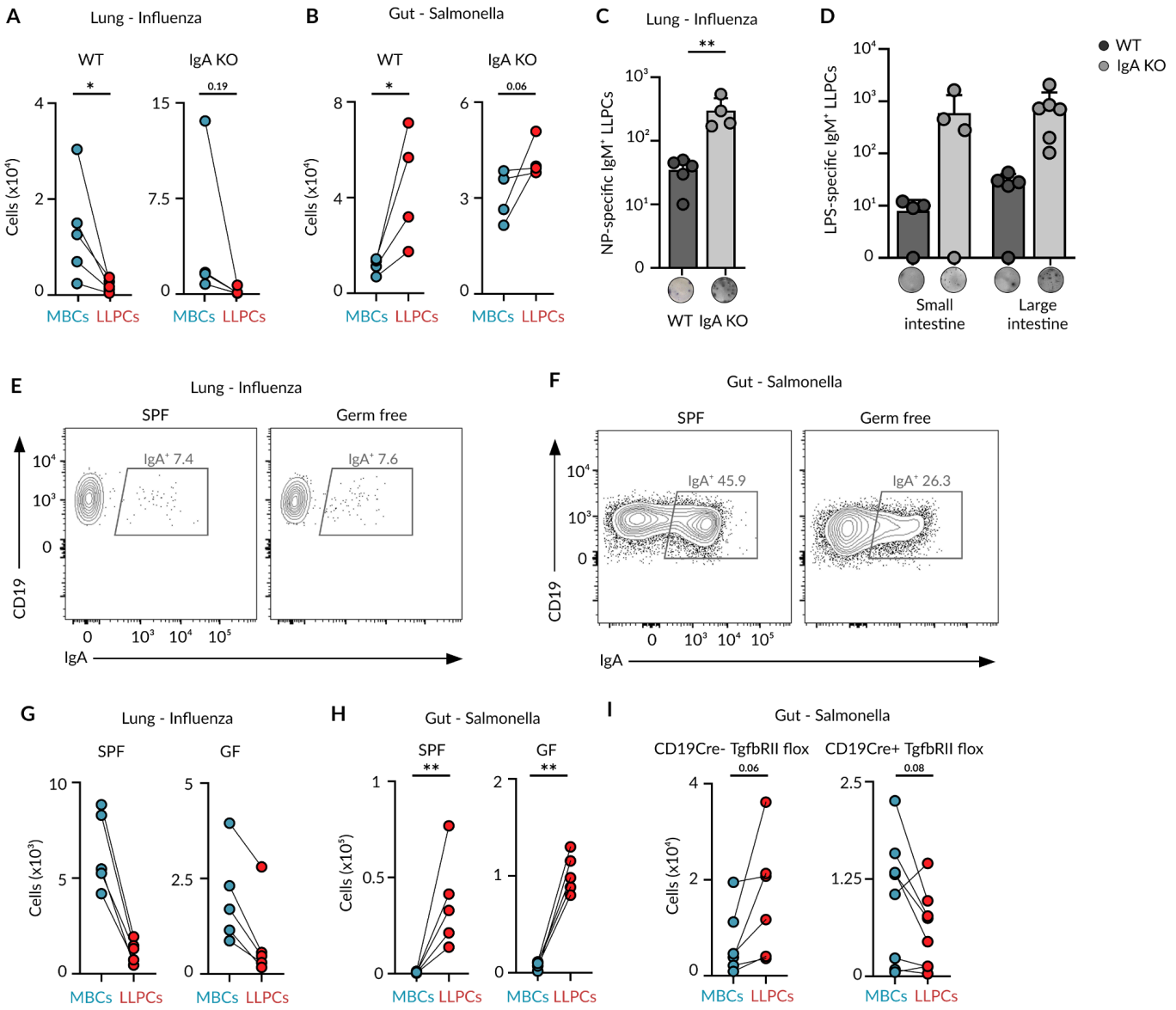

Figure S5. Regulation of mucosal B cell memory by the microbiota-TGFβ-IgA axis. (**A**-**B**) Quantification of MBC and LLPC numbers in (A) lungs of influenza-infected and (B) gut of *Salmonella*-infected wild type and *Igha* KO mice (day 35). (**C**) Enumeration of lung NP-specific IgM⁺ antibody-secreting cells in influenza-infected wild type and *Igha* KO mice by ELISpot. (**D**) Enumeration of gut LPS-specific IgM⁺ antibody-secreting cells in *Salmonella*-infected wild type and *Igha* KO mice by ELISpot. (**E**-**F**) Flow cytometry plots display IgA expression by GC B cells in (**E**) lungs of influenza-infected and (**F**) gut of *Salmonella*-infected SPF and GF mice. (**G**-**H**) Quantification of MBC and LLPC numbers in (G) lungs of influenza-infected and (H) gut of *Salmonella*-infected SPF and GF mice (day 35). (**I**) Quantification of MBC and LLPC numbers in gut of *Salmonella*-infected CD19-cre Tgfbr2$^{fl/fl}$ mice (day 35). In all panels, quantifications display one representative experiment, mean ± s.e.m. Each dot represents one mouse. t test: *p<0.05 and **p<0.01.

Figure S6

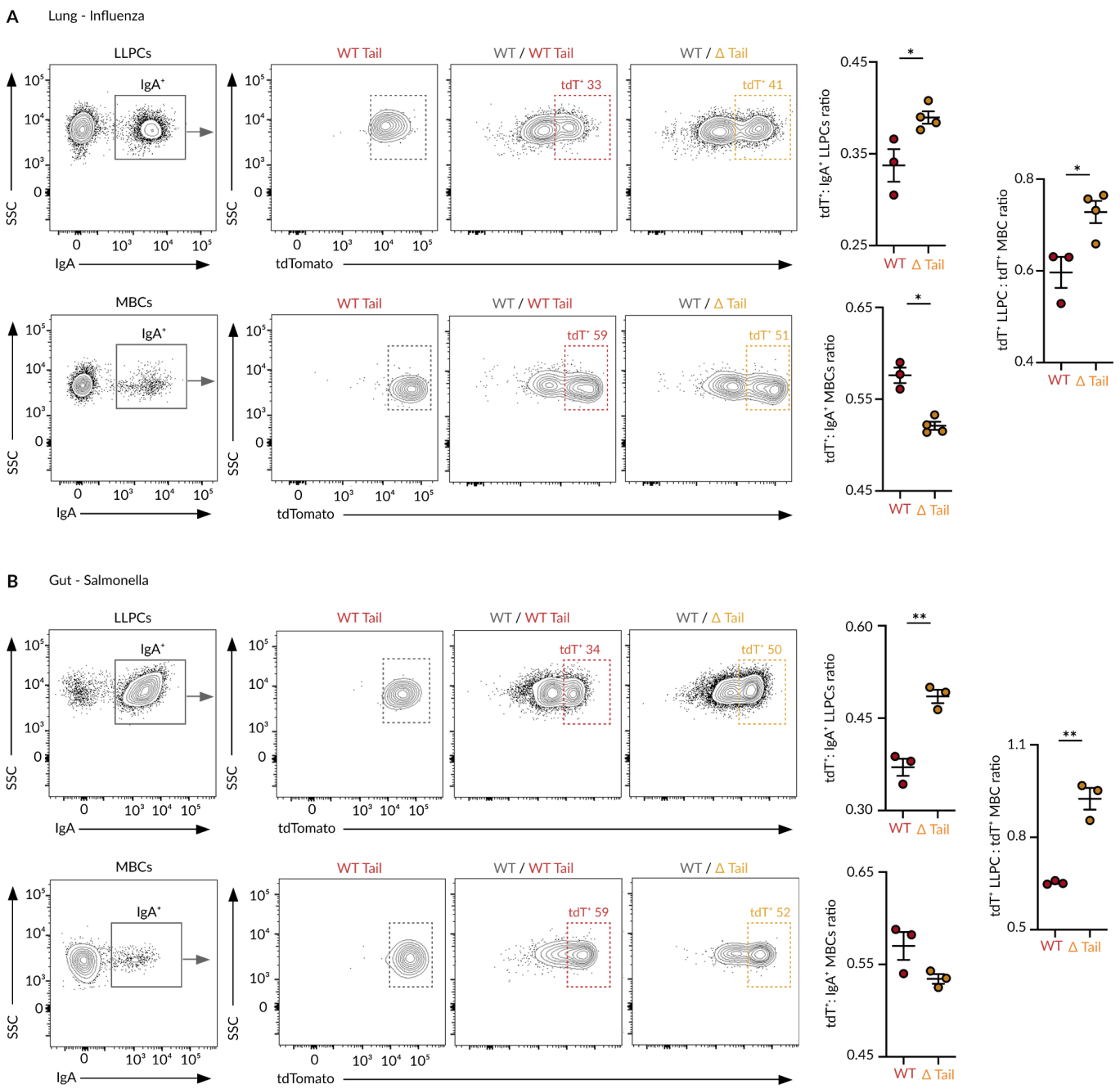

Figure S6. Mucosal B cell memory instruction by the IgA cytosolic tail in a competitive system. (**A-B**) Contour plots displaying tdTomato expression by IgA$^+$ MBCs and LLPCs in (A) lungs and (B) gut of Igha-tdTom$^{+/+}$, Igha-tdTom$^{+/-}$ and Igha-Δtail-tdTom$^{+/-}$ mice infected with (A) influenza virus or (B) *Salmonella*, respectively (day 35). Quantifications show tdT$^+$:IgA$^+$ ratios for LLPCs and MBCs. In all panels, quantifications display one representative experiment, mean ± s.e.m. Each dot represents one mouse. t test: *p<0.05 and **p<0.01.

Methods

Mice

8-week old wild-type SPF C57BL/6 and BALB/cJRj mice were obtained from Janvier Labs. Aicda-CreERT2 mice were obtained from Claude-Agnès Reynaud and Jean Claude Weill, Institut Necker Enfants Malades, France. Rosa26-EYFP mice were obtained from Jackson Laboratories, USA. CD19-Cre mice were obtained from Sandrine Roulland, Centre d'Immunologie de Marseille Luminy, France. Igha-KO mice were obtained from Emma Slack, Institute of Food, Nutrition and Health, Switzerland. Tgfbr2$^{fl/fl}$ mice were obtained from Julien Marie, Cancer Research Center of Lyon, France. Aid(G23S) mice were obtained from Tasuku Honjo, Center for Cancer Immunotherapy and Immunobiology, Japan. α1KI mice were obtained from Michel Cogné, Laboratoire d'Immunologie, Université de Limoges, France. CD23cre Bcl6$^{fl/fl}$ mice were obtained from Michelle Linterman, Babraham Institute, UK. Aicda-Cre^{ERT2} mice were further crossed with Rosa26-EYFP mice. IgA-tdT mice (C57BL/6NRj-Igha^{tm1Ciphe}) and Igha-Δtail-tdTom (C57BL/6NRj-Igha^{em2Ciphe}) were generated in CIPHE (Centre d'Immunophénomique). Igha-tdTom mice were generated by homologous recombination in embryonic stem cells. Igha-Δtail-tdTom were obtained by deletion of Igha tail by electroporation of CRISPR/Cas9 complex and single-stranded donor DNA into homozygous zygotes for the Igha-tdT mice. Germ-free C57BL/6 mice were purchased from TAAM-CNRS (Orléans, France).

Mice were bred and maintained at the animal facilities of the Centre d'Immunologie de Marseille Luminy and Ciphe. Up to five mice per cage were housed under a standard 12 hr light/dark cycle, with room temperature at 22°C (19°C-23°C change). They were fed with autoclaved standard pellet chow or tamoxifen pellet chow when indicated, and reverse osmosis water. All cages contained 5 mm of aspen chip and tissue wipes for bedding and a mouse house for environmental enrichment. Mice were used at the age of 8 to 12 weeks and littermates (males or females) were randomly assigned to experimental groups. Generally between 4 to 5 mice were used per experimental group. Experimental procedures were conducted in accordance with French and European guidelines for animal care under the permission number 16708-2018091116493528 and 43129-202304171838427 following review and approval by the local animal ethics committee in Marseille.

Infections and injections

For intranasally infections, mice were anesthetized i.p. with Ketamine/Xylazine (100 mg/kg body) and intranasally infected with 5 PFU of Influenza virus A/Puerto Rico/8/1934 (PR8) H1N1 strain, $5x10^4$ PFU of Influenza virus A/X-31 H3N2, 10^7 CFU of *Klebsiella pneumoniae* 43816 strain or $5x10^3$ CFU of *Klebsiella pneumoniae* 52145 strain in 20 µl of PBS. Influenza virus was amplified on MDCK cells. Purification of viral particles was performed in a sucrose 30% cushion at 25,000 RPM for 2 hours in an SW32Ti rotor. For Aid-EYFP mice, tamoxifen (Cayman chemical) was resuspended in corn oil (Sigma), sonicated and given by oral gavage at 5mg/100µl. For gastrointestinal infections, mice were orally gavaged with 10^{10} CFU of *Salmonella typhimurium* aroA SL3261, $5x10^6$ CFU *Salmonella* WT or 10^{10} CFU of *Klebsiella pneumonia*e 43816 strain in 100 ul of PBS with a reusable feeding needle. *Salmonella typhimurium aro*A SL3261 and WT strains were obtained from David Holden, Imperial College London, UK. *Klebsiella pneumoniae* was obtained from Régis Tournebize, Institut Pasteur, France. For *in vivo* labeling of immune cells in circulation, 3 µg of anti-CD45 antibody was administered i.v 5 minutes before sacrifice.

Flow Cytometry

For isolation of lamina propria cells, the intestine was divided into small and large sections. Peyer's patches and caecum were excised from small and large intestine respectively, and processed afterwards. Small and large intestines were opened longitudinally and incubated in HBSS 2mM EDTA twice (1x 20 min and 1 x 30 min) at 37°C to remove epithelial cells. Then, cells were washed twice with HBSS $Ca^{+2}Mg^{+2}$ and incubated

for 25 (small intestine) or 35 min (large intestine) in RPMI 1640 with 10% FCS, 1mg/ml of collagenase IV (Sigma), DNAse I 30ug/ml. The reaction was stopped with 1:100 of 0.5M EDTA, filtered consecutively through 100- and 70-µm mesh and the cell suspension was finally purified by density gradient centrifugation with 40–80% Percoll (GE Healthcare). Single cell suspensions of Peyer's patches, mediastinal or mesenteric lymph nodes and spleens were obtained by pressing organs through a 70µm nylon mesh cell strainer with a plastic plunge in PBS 2%FCS 5mM EDTA. For lungs, single cell suspensions were obtained with the mouse lung dissociation kit (Miltenyi) according to manufacturer instructions and lymphocytes were enriched by using 40-80% Percoll gradient. For spleen and lungs, cell suspensions were further incubated with a red blood cell lysis buffer for 5 minutes. To block nonspecific antibody binding, cell suspensions were incubated with hybridoma supernatant 2.4G2 diluted 1/4 in PBS 2%FCS 5mM EDTA and when indicated with LIVE/DEAD Fixable Blue Dead Cell Stain Kit (Thermo Fisher Scientific) to exclude dead cells, for 20 minutes on ice. For cell death assay, 1 x 10^6 cells were stained with NucView® Caspase-3 Enzyme Substrates (Biotium, 10402) during 30 minutes at room temperature. Regarding ROS measurement, 1 x 10^7 cells were cultured overnight with 400µL of complete RPMI medium, containing or not anti-IgA (SouthernBiotech, 10µg/mL). Cells were then stained with 100µL of MitoSox green (ThermoFischer, 5µM) diluted in FACS buffer, during 30 minutes at 37°C. For labeling of surface markers, cells were stained for 20 minutes on ice with the indicated anti-mouse antibodies. When indicated, cell suspensions were fixed 30 minutes with PFA 4%. Intracellular staining was performed with Cytofix/Cytoperm Fixation/Permeabilization Kit (BD Biosciences) following manufacturer protocol. Finally, cells were either resuspended in 400µl of PBS 2%FCS 2mM EDTA together with the addition of beads (CountBright™ Absolute Counting Beads, Invitrogen) and analyzed on Fortessa-X20/Symphony/LSRIIUV cytometers (BD Biosciences) or in complete RPMI medium (FCS 10%, Penicillin 100µg/ml, Streptomycin 10µL/ml, Sodium Pyruvate 1mM, 50µM 2-mercaptoethanol) and used for cell sorting on a FACSAria II (BD, Bioscience). For non-fixed cells, a mix of counting beads and DAPI (0.1 µg/ml final concentration) was added right before passing samples on cytometers. Data was analyzed using FlowJo (TreeStar).

Antibody	Source	Catalog
Alexa Fluor 488 anti-mouse IgG2b Antibody, Clone RMG2b-1	Biolegend	406718
Alexa Fluor 647 Goat Anti-Mouse IgA, polyclonal	Southern BT	1040-31
Alexa Fluor 647 Rat Anti-Mouse Bcl-6, clone K112-91	BD Horizon	561525
Alexa Fluor 647 Goat anti-Mouse IgG2a Cross-Adsorbed Secondary Antibody, polyclonal	ThermoFisher	A-21241
Alexa Fluor 647 Rat Anti-Mouse/Human GL7 Antigen, Clone GL7	Biolegend	144606
APC CD90.1 (Thy-1.1), CloneHIS51	ThermoFisher	17-0900-82
APC/Cy7 Rat Anti-Mouse CD19, Clone 6D5	Biolegend	115530
BUV395 Rat Anti-Mouse CD45R/B220, clone RA3-6B2	BD Horizon	563793
BUV395 Rat Anti-Mouse CD38, Clone 90/CD38	BD Horizon	740245
BUV737 Rat Anti-Mouse CD98, Clone H202-141	BD	749412
BUV737 Rat anti-Mouse/Human CD45R (B220), Clone RA3-6B2	BD Horizon	612839
BV421 Armenian Hamster Anti-Mouse CD183 (CXCR3), Clone CXCR3-173	Biolegend	126522

BV510 Rat Anti-Mouse CD138 (Syndecan-1), Clone 281-2	Biolegend	142521
BV510 Rat Anti-Mouse CD45, Clone 30-F11	Biolegend	103138
BV510 Rat Anti-Mouse Ig, κ light chain, Clone 187.1	BD	742834
BV605 Armenian Hamster Anti-Mouse CD95 (Fas), Clone Jo2	BD Horizon	740367
BV650 Rat Anti-Mouse CD93, Clone AA4.1	BD	563807
BV650 Rat Anti-Mouse IgG3, Clone R40-82	BD	744136
BV711 Rat Anti-Mouse CD138 (Syndecan), Clone 281-2	Biolegend	142519
BV785 Rat Anti-Mouse CD138 (Syndecan-1), Clone 281-2	Biolegend	142534
BV786 Rat Anti-Mouse IgD, Clone 11-26c.2a	BD Horizon	563618
FITC Goat Anti-Mouse IgG2c (heavy chain), polyclonal	Abcam	ab97254
FITC Mouse Anti-Mouse CD95 (Fas), Clone SA367H8	Biolegend	152606
FITC Rat Anti-Mouse CD45, Clone 30-F11	Biolegend	103108
FITC Rat Anti-Mouse/Human GL7 Antigen, Clone GL7	Biolegend	144604
Pacific Blue Rta Anti-Mouse/Human GL7, clone GL7	Biolegend	144614
PE Mouse Anti-Human IgA, clone IS11-8E10	Milteny	130-114-002
PE Rat Anti-Mouse CD138 (Syndecan-1), Clone 281-2	Biolegend	142504
PE Rat Anti-Mouse CD98 (4F2), clone RL388	Biolegend	128208
PE Rat Anti-Mouse IgA, clone mA-6E1	eBioscience	12-4204-82
PE Rat Anti-Mouse IgG2b, Clone RMG2b-1	Biolegend	406708
PE Mouse Anti-Mouse/Human Btk (pY223), Clone N35-86	BD	562753
PE/Cyanine7 Rat Anti-Mouse IgD, Clone 29-2L17	Biolegend	405720
PE/Cyanine7 Rat Anti-Mouse CD39 Antibody, clone Duha59	Biolegend	143805
PE/Cyanine7 Rat Anti-Mouse CD98 (4F2), clone RL388	Biolegend	128214
PE/Cyanine7 Rat Anti-Mouse IgG2b, clone RMG2b-1	Biolegend	406713
PE/Dazzle594 Hamster Anti-MouseCD196 (CCR6), Clone29-2L17	Biolegend	129822
PerCP/Cyanine5.5 Rat Anti-Mouse IgM, Clone RMM-1	Biolegend	406512
PerCP/Cyanine5.5 Rat Anti-Mouse/Human GL7, clone GL7	Biolegend	144610
V450 Rat Anti-Mouse IgG1, Clone A85-1	BD	562107
Alexa Fluor 555 Goat Anti-Rabbit IgG (H+L)	ThermoFisher	A-21428
Rabbit anti RFP, Polyclonal	ThermoFisher	600-401-379

Biotinylated Goat Anti-Mouse IgA, polyclonal	Southern BT	1040-08
Biotinylated Goat Anti-Mouse IgG, polyclonal	Southern BT	1030-08
Biotinylated Goat Anti-Mouse IgG2c, polyclonal	Southern BT	1079-08
Biotinylated Goat Anti-Mouse IgM, polyclonal	Southern BT	1020-08
Goat F(ab')2 Anti-Mouse Kappa-UNLB	Southern BT	1052-01
APC/Cyanine7 Streptavidin	Biolegend	405208

Immunohistochemistry

Lungs were fixed in 4% PFA for 6 hours at 4°C. Small and large intestines were opened longitudinally, washed with PBS and fixed with PFA 4% for 30 min at 4°C. Afterwards, intestines were washed with PBS and swiss rolls were made and fixed again for another 30 mins. After washing, lungs, lymph nodes and intestines were washed with PBS, incubated overnight in PBS 30% sucrose solution, immersed in OCT and snap-frozen in liquid nitrogen-cooled isopentane. Cryostat sections (10 to 20 µm thick) were dried in silica beads, permeabilized with PBS Saponin 0.5% for 30 minutes and blocked with PBS 0.5% saponin 2% BSA 1% goat serum 1% FCS for 30 minutes. Sections were then incubated with primary antibodies in PBS 0.5% saponin 2% BSA 1% goat serum 1% FCS for at least 1 hour, washed and incubated with secondary antibodies for a further hour. After a final wash, sections were mounted in Fluoromount-G mounting media. Imaging was carried out on a LSM 780 (Zeiss) inverted confocal microscope using a Plan-Apochromat 40x NA 1.3 oil immersion objective or a Plan-Apochromat 20X/0.8 M27 objective in the case of full organ section.

Antibody	Source	Catalog
Alexa Fluor 647 Rat Anti-Mouse Bcl-6, clone K112-91	BD Horizon	561525
Pacific Blue Rat Anti-Mouse/Human CD45R (B220), Clone RA3-6B2	Biolegend	103227
PE Rat Anti-Mouse CD138 (Syndecan-1), Clone 281-2	Biolegend	142504
Chicken Anti-GFP, polyclonal	Abcam	ab13970

Analysis of confocal images

After collecting tile scans by confocal microscopy, lung sections were analyzed using Imaris 9.6.0 software. The Surface Creation Wizard was used to identify the YFP positively stained cells based on fluorescence intensity, size and morphology. The selection parameters were established as follows: source channel set to yellow (YFP), smooth: 2, thresholding - background subtraction: 5, threshold: 7, split: 1 and area: 50 µm. Once identified, a value-based visual surface was generated for all positively stained cells, which enabled quantification of fluorescence intensity as well as the frequency of labeled and unlabeled cells. Channel statistics for B220, Bcl-6 and CD138 were obtained for cellular surfaces defined based on YFP+ cells and exported into Excel (Microsoft). Mean voxel fluorescence was plotted in FlowJo software by using the Text to FCS conversion utility (TreeStar Inc). Percentages of YFP+ for B220, GL7 or CD138 were gated using traditional log-scale based flow cytometry plots in FlowJo and then graphed on linear XY plots to map their respective positions within the lung.

ELISPOT

To measure specific antibody-secreting cells, enzyme-linked immunosorbent spot (ELISpot) multiscreen filtration plates (Millipore) were activated with absolute ethanol, washed with PBS and coated overnight at 4°C with 1µg/ml of nucleoprotein or hemagglutinin (Sino Biological) or 5 µg/ml of Salmonella- or Klebsiella-LPS (Sigma-Aldrich) diluted in PBS. Plates were subsequently blocked for 1 hour with complete medium and incubated for 24 hours at 37°C with serial dilutions of lung, bone-marrow, small and large intestine single cell suspensions. Plates were washed with PBS 0.01% Tween-20 and incubated for 1 hour with 1µg/ml of biotinylated anti-IgM, IgG, IgA or total Ig (Southern Biotech) diluted in PBS 1% BSA. Then, plates were washed and incubated for 30 minutes with 1µg/ml Streptavidin-Alkaline Phosphatase (Sigma). Finally, plates were washed and developed with BCIP®/NBT (Sigma).

Fecal extract

Fecal pellets were collected at indicated times, snap-frozen and stored at −80°C until analysis. Fecal pellets were resuspended in PBS 10% FCS at a ratio of 10 mg per 100 µl, vortexed for 20 min to disrupt pellets at 4°C and centrifuged 10 min at 13,000 x g. Supernatants were collected and stored at -20°C for subsequent analysis.

ELISA

To measure the production of specific antibodies, ELISA (enzyme-linked immunosorbent assay) plates were coated overnight at 4°C with either 1µg/ml of hemagglutinin (Sino Biological) or 5 µg/ml of Salmonella LPS (Sigma) diluted in PBS. Plates were washed with PBS 0.01% Tween, blocked for 1 hour at room temperature with PBS 1% BSA and incubated overnight at 4°C with serial dilutions of serum or fecal extract. The following day, plates were washed and probed at room temperature for 1 hour with 1µg/ml of biotinylated anti-IgA or -IgG (Southern Biotech) in PBS 1%BSA. Plates were washed and incubated at room temperature for 30 minutes with 1µg/ml Streptavidin-Alkaline Phosphatase (Sigma). Plates were washed and developed with p-NitrophenylPhosphate (Sigma). 405 nm absorbance was detected using a SPECTRAmax190 plate reader (Molecular Device).

Gene-expression analysis

Total RNA was extracted using the RNeasy® Mini Kit (Qiagen, Hilden). The reverse transcription into the cDNA was performed with SuperScript II (Invitrogen). The expression of Tgfb1 relative to Actb was measured by real-time PCR (95°C 3 m 1 cycle; 95°C 5 s; 60°C 34 s, 40 cycles, 95°C 15 s, 50°C 1 m 1 cycle) with the StepOnePlus (Applied Biosystems) using ONEGreen® Fast qPCR Premix and the following primers:
- Tgfb1 (Fw: 5´-CACAGCTCACGGCACCGGAGA-3´; Rv: 5´-GCTGTACTGTGTGTCCAGGCTCC-3´)
- Actb (Fw: 5´-CTCCTGAGCGCAAGTACTCTGTG-3´; Rv: 5´-TAAAACGCAGCTCAGTAACAGTCC-3´).

A20 class switching and Igha tail deletion

A20 B cells were grown in complete RPMI medium. Guide RNAs (gRNA) were used to induce IgG2a to IgA class switching. Sγ2a 3′ gRNA was designed to target the region between the switch Sγ2a sequence and the constant region Cγ2a sequence. Sα3′ gRNA was designed to target between the switch Sα sequence and the constant region Cα sequence. (Sγ2a 3'gRNA: 5'-TGGCAACATTAGCGCTATCA-3'; Sα3′ gRNA: 5'-GGCTGGAATTAGGCGAAACT-3'). 22 pmoles of Sγ2a 3′ gRNA were coupled to 18 pmoles Cas9-GFP (IDT) to form ribonucleoprotein (RNP1). In the same proportions, Cas9-RFP (IDT) was folded with Sα3′ gRNA to form RNP2. RNP1 was mixed with RNP2 in 1:1 ratio and then added to $2x10^6$ A20 cells, resuspended in an electroporation buffer contained in Cell Line Nucleofector Kit V (Lonza). A20 cells were

electroporated (Amaxa Nucleofector II/2b, Program L-013) and sorted one to three days later in a BD FACSAria II (BD, Bioscience). IgA^+ A20 cells were screened for BCR expression by using goat anti-mouse IgG2a (ThermoFisher Scientific, 10µg/mL) and anti-mouse IgA (mA-6E1, eBioscience, 1µg/mL).

Control Igha wild type tail and Igha deleted tail were obtained by using one gRNA targeting endogenous Igha tail (5'-AGGCCCGTTTGGCAGCAAAG-3') and a double strand donor DNA (TWIST Bioscience) to allow homologous recombination and selection. The donor DNA contains 5' to 3': 5' homology arm/ wild type or deleted Igha tail/ three amino-acid linker/ P2A sequence/ cd90.1 cDNA/ 3' homology arm. Homozygous recombinants were screened on 5' and 3' side by PCR using the following primers:
5' Fw : 5'-TCAAGAACTGCTGGGATTCCAGTCCCT-3'
5' Rv1 : 5'-CATCCTGGAGTTGGGTTATGTCTTCCCTTT-3'
5' Rv2 : 5'-AGGCTGTCAGGCTGGTCACCTTCTGCC-3'
3' Fw1 : 5'-TCAAGAACTGCTGGGATTCCAGTCCCT-3'
3' Fw2 : 5'-CATCCTGGAGTTGGGTTATGTCTTCCCTTT-3'
3' Rv : 5'-GAGTTTGTGGTTTTGCATCAATTTATT-3'

Phospho-flow cytometry

2×10^6 cells were stained with the LIVE/DEAD Fixable Blue Dead Cell Stain Kit (Thermo Fisher Scientific) for 20 minutes on ice. The cells were plated in 100 µL of RPMI with 2% FCS for 1 hour at 4°C and then stimulated at 37°C with 10 µg/mL Goat anti-mouse IgA (SouthernBiotech) in 100 µL of RPMI with 2% FCS. Cells were fixed for 10 minutes at 37°C and 20 minutes on ice with 200 µL of Fixation/Permeabilization solution (FoxP3/Transcription Factor Fixation and Permeabilization buffer, eBioscience, Invitrogen). Cells were washed with 150 µL of Permeabilization buffer and incubated with 25 µL of hybridoma supernatant 2.4G2, diluted 1:4 in Permeabilization buffer, for 15 minutes on ice. Then, the cells were incubated for an additional 30 minutes on ice with the indicated anti-mouse antibodies. Cells were washed twice and incubated with PE Mouse anti-Btk (pY223) (N35-86, BD Phosflow, 1 µg/mL) or anti-Syk (pY348) (558529, BD Phosflow, 1 µg/mL) for 30 minutes at room temperature in the dark, washed with PBS containing 2% FCS, and analyzed using an LSRIIUV cytometer

Calcium measurement

8×10^6 cells were loaded with 5 µM Indo-1 (Invitrogen) in RPMI with 10 mM HEPES (pH 7) for 30 minutes at 37°C. The cells were then incubated with RPMI containing 10 mM HEPES (pH 7.4) and 5% FCS in a 1:1 proportion at 37°C for 30 minutes, followed by a wash with RPMI containing 5% FCS. Calcium flux was measured using an LSRIIUV cytometer. The baseline (bound/unbound) was acquired for 1 minute, after which the cells were stimulated with anti-IgA (SouthernBiotech) at indicated concentrations, and calcium flux was acquired for 5 minutes. Ionomycin (Sigma-Aldrich) was then added at a concentration of 5 µg/mL, and calcium flux was measured for an additional 5 minutes.

Western blot

10×10^6 cells were plated in 100 µL of RPMI and incubated for 1 hour at 4 °C. Cells were then stimulated at 37 °C with 40 µg/mL of goat anti-mouse IgA (SouthernBiotech) in 100 µL of RPMI. Following stimulation, cells were lysed on ice for 30 minutes with 400 µL of 2× lysis buffer (100 mM Tris-HCl pH 7.4, 1 mM EDTA, 1% n-dodecyl-β-D-maltoside, 274 mM NaCl, 20% glycerol), supplemented with protease and phosphatase inhibitors: leupeptin (20 µg/mL), aprotinin (20 µg/mL), PMSF (20 µg/mL), TPCK (20 µg/mL), TLCK (20 µg/mL), sodium orthovanadate (Na_3VO_4, 2 mM), and sodium fluoride (NaF, 100 mM). Lysates were cleared by centrifugation at maximum speed for 15 minutes at 4 °C. Supernatants were collected, and protein concentrations were determined using the Bradford assay. Equal amounts (80 µg) of protein per sample were mixed with Laemmli buffer containing 10% β-mercaptoethanol, boiled for 5 minutes at 95 °C,

and loaded onto SDS-PAGE gels. Proteins were separated by electrophoresis at 150 V and then transferred onto PVDF membranes at 40 V for 2 hours. Membranes were blocked overnight at 4 °C in 5% BSA in TBS-T (Tris-buffered saline with 0.1% Tween-20), then incubated with primary antibodies: Anti-Phosphotyrosine Antibody, clone 4G10 (05-321, Sigma) or anti-β-actin diluted in 5% BSA in TBS-T for 2 hours at room temperature or overnight at 4 °C. After washing, membranes were incubated with HRP-conjugated secondary antibodies for 1 hour at room temperature. Detection was performed using enhanced chemiluminescence (ECL) reagents and visualized with a chemiluminescence imaging system.